Influence of trace level As or Ni on pyrite formation kinetics at low temperature

C. Baya, Pierre Le Pape, B. Baptiste, J. Brest, G. Landrot, E. Elkaïm, V. Noël, M. Blanchard, G. Ona-Nguema, F. Juillot, et al.

To cite this version:

C. Baya, Pierre Le Pape, B. Baptiste, J. Brest, G. Landrot, et al.. Influence of trace level As or Ni on pyrite formation kinetics at low temperature. Geochimica et Cosmochimica Acta, 2021, 300, pp.333-353. ⟨10.1016/j.gca.2021.01.042⟩. ⟨hal-03164649⟩

HAL Id: hal-03164649
https://hal.science/hal-03164649v1

Submitted on 10 Mar 2021

Influence of trace level As or Ni on pyrite formation kinetics at low temperature

Baya C.[1], Le Pape P.[1]*, Baptiste B.[1], Brest J.[1], Landrot G.[2], Elkaïm E.[2], Noël V.[3], Blanchard M.[4], Ona-Nguema G.[1], Juillot F.[1,5], Morin G.[1]

1. Institut de Minéralogie, de Physique des Matériaux et de Cosmochimie (IMPMC), UMR 7590 CNRS-Sorbonne Université-IRD-MNHN, case 115, 4 place Jussieu, 75252 Paris Cedex 5, France.

2. Synchrotron SOLEIL, F-91192 Gif Sur Yvette, France

3. Stanford Synchrotron Radiation Lightsource, SLAC National Accelerator Laboratory, 2575 Sand Hill Road, MS 69, Menlo Park, CA 94025, USA

4. Géosciences Environnement Toulouse (GET), Université de Toulouse, CNRS, IRD, UPS, CNES, 14, Avenue Edouard Belin, 31400 Toulouse, France.

5. Institut de Recherche pour le Développement (IRD), UMR 206/UMR 7590 IMPMC, 98848 Nouméa, New Caledonia

January, 10th 2021,
Revised version submitted to
Geochimica et Cosmochimica Acta

***Corresponding author**: pierre.le_pape@upmc.fr

ABSTRACT

Pyrite formation at low temperature during early diagenesis in (sub-)surface sediments is an essential step of Fe and S biogeochemical cycles and the presence of this ubiquitous mineral of surface environments is often used as an indicator of paleo-redox conditions. Pathways of pyrite formation are usually discussed in environmental settings by involving a variety of nanosized Fe-S mineralogical precursors as a function of the local geochemical conditions. However, the influence of trace element impurities such as Ni and As in the solution at the time of pyrite formation has been poorly studied, whereas specific chemical signatures of trace elements are commonly observed in sedimentary pyrites. A better understanding of the impact of Ni and As incorporation at trace levels on pyrite formation is essential to help refining the use of these elements as paleo-redox indicators and to evaluate the role of pyrite as a sink regulating the biogeochemical cycle of potentially toxic trace elements. In this study, we have performed syntheses of pyrite at low temperature by the polysulfide pathway using aqueous Fe(III) and H_2S in the presence of trace amounts of Ni(II) (0.001 mol%Fe) and As(III) (0.001 mol%Fe). Analysis of the solids collected at different time steps over the course of the experiments using X-Ray absorption spectroscopy at both the Fe and S *K*-edges shows that pyrite starts to precipitate within 5 days in presence of Ni(II) and within 32 days in presence of As(III), while the control experiment showed an intermediate precipitation rate of 14 days. Shell-by-shell analysis of Fe *K*-edge EXAFS data shows that the initial mineralogical precursors are the same whatever the experimental conditions and correspond to poorly-crystalline FeS (3.0±0.1 Fe-S@2.25 Å; 1.7±0.2 Fe-Fe@2.67 Å). In addition, XANES qualitative analysis suggests the incorporation of small amounts of Fe(III) within these FeS precursors. Synchrotron-based XRD and WAXS-PDF analysis of the starting solids show that in addition to S(0), the FeS precursors correspond to a continuum of FeS particles that ranges from tetragonal nanocrystalline FeS (a = 3.70(2) Å, c = 5.24(7) Å, MCD_{ab} = 41±4 Å MCD_c = 21±2 Å) to cluster-type FeS (MCD_{abc} < 8.4±4.3 Å). We propose that Ni(II) and As(III) have a different type of interaction with these FeS precursors, resulting respectively in an increase and a decrease in the rate of pyrite nucleation. While Ni(II) would incorporate within the structure of the FeS precursors, As would interact with (poly)sulfides in solution to form thio-As, possibly binding or precipitating onto FeS surfaces and thus slowing FeS transformation to FeS_2. Given that both Ni and As were introduced at trace levels in our experiments, these results suggest that the occurrence of trace amounts of impurities could have a strong influence on pyrite precipitation kinetics in natural settings such as pore-scale microenvironments. In addition to emphasizing the importance of trace elements such as Ni or As on the persistence of mobile colloidal FeS species in anoxic conditions, the results of the present study also point to the importance of considering the actual nature of the impurities when using pyrite composition for ancient environments and past climates reconstruction.

Keywords: pyrite, nickel, arsenic, incorporation, kinetics, precursors, iron sulfides, mackinawite, paleo-environments, contaminants, trace elements.

INTRODUCTION

Pyrite (FeS_2) occurs frequently in marine and, to a lesser extent, continental sediments (Rickard and Morse, 2005; Rickard and Luther, 2007) and is known for its ability to trap trace elements such as Ni, As, Zn, Pb, Se and Co (Huerta-Diaz and Morse, 1992; Zhang *et al.*, 2002; Thomas *et al.*, 2011; Large *et al.,* 2012; Large *et al.,* 2017). Thus, pyrite trace element composition have been used as indicator for trace element abundance in ancient environments, providing information on major past geological and climatic events that have affected Earth's history (Gregory *et al.,* 2017). Large *et al*. (2017) have proposed that trace element contents in marine pyrite could record the chemical composition of seawater at the time of precipitation, For instance, Large *et al.* (2014) have used the geochemical compositions of pyrite in sedimentary archives to propose that erosion of Ni- and Co-rich komatiitic Large Igneous Provinces (LIPs) from the Archean have contributed to the high levels of Ni and Co in the global ocean. Such reconstructions depend on the ability of pyrite composition to mirror that of the solution, which eventually depends on complex elemental partition coefficient at the solid-solution interface. Although conditional affinities of trace elements for pyrite can be derived from natural and experimental data (Large *et al.*, 2014), further elucidation of the actual mechanisms and parameters that control trace element incorporation in pyrite could help to improve the use of this mineral as a proxy for the paleo-chemistry of ancient sedimentary environments. Additionally, recent studies using machine learning algorithms suggest that patterns of trace element content in pyrite could be used as potential markers of biosignatures (Figueroa *et al*., 2017), which can be a powerful approach to decipher among past biotic/abiotic processes.

Among the factors that are known to influence trace element incorporation in pyrite, Tribovillard *et al.* (2006) and Konhauser *et al*. (2011) have shown that the redox conditions that prevailed during pyrite formation can influence the incorporation of redox-sensitive elements, since homovalent substitution is favoured in the pyrite structure. Thus, variations in the abundance of redox-sensitive elements such as Se or Mo in pyrite have been used as markers of past changes in the oxygenation of ancient atmospheres and oceans (Mukherjee *et al.*, 2019). However, Tribovillard (2020)'s recent work has questioned the use of As as a redox proxy since the occurrence of sulfidic reducing conditions are not globally correlated with As enrichment in marine sediments. In this context, a better understanding of the mechanisms of trace element incorporation in pyrite is essential for refining paleo-environmental models. To this regard, recent experimental studies have highlighted that metal or metalloid impurities in the aqueous medium can largely influence the kinetics of pyrite precipitation, with major effects on the solid to solution partition coefficient for these elements and on their modes of incorporation in the pyrite crystals. In particular, Morin *et al.* (2017) have shown that aqueous Ni in the synthesis solution accelerates pyrite formation at ambient temperature, via the nucleation of Ni-rich pyrite crystallites that forms the core of resulting pyrite nanocrystals. This process leads to a major enrichment in Ni over Fe in pyrite compared to the Ni/Fe ratio of the synthesis solution. Besides, Le Pape *et al.* (2017) have reported that the presence of aqueous arsenite, in the form of H_3AsO_3 arsenious acid, slows down pyrite formation at ambient temperature in acidic conditions and that arsenic is incorporated as $As^{II,III}$ and As^{-I} at the Fe(II) and S^{-I} sites, respectively, in the pyrite structure. Such kinetic effects are particularly significant at low temperature and may thus be relevant to early-diagenetic processes occurring in marine and continental sediments. However, further work is needed to elucidate the mechanisms that cause these kinetic effects and to evaluate their importance in natural media.

At the mechanistic level, primary issues to be addressed are the unknown relations between these kinetic effects and the possible mechanisms of pyrite nucleation and growth at low temperature. Different reaction pathways have been proposed, which may involve solid precursors such as amorphous iron monosulfide (FeS), mackinawite (FeS_m), greigite (Fe_3S_4) (Benning *et al.*, 2000; Rickard and Luther, 2007) and elemental sulfur, as well as aqueous precursors such as Fe_xS_x polymeric species, polysulfides (S_n^{2-}) and H_2S_{aq} (Rickard, 1975; Rickard and Luther, 2007). Iron monosulfide (FeS) is a classical precursor for pyrite in concentrated media used for experimental pyrite syntheses (Berner, 1970; Wilkin and Barnes, 1996; Benning *et al.*, 2000; Neretin *et al.*, 2004; Rickard and Luther, 2007). It is considered to be in equilibrium with dissolved/colloidal Fe_xS_x that may be the actual precursor of pyrite in natural dilute media (Rickard and Morse, 2005). Rickard (1975) and Rickard and Luther (2007) have also demonstrated that aqueous polysulfide species (*e.g.* H_2S_2, HS_2^-, S_2^{2-}, S_n^{2-}), that can derive from dissolution of elemental sulfur in concentrated synthesis media, play a major role in pyrite formation. Thus, two main mechanisms involving the reaction of nano-crystalline FeS_m or dissolved/colloidal Fe_xS_x with polysulfides (Rickard, 1975; Luther, 1991) or with aqueous H_2S (Rickard, 1997; Rickard and Luther, 2007) are usually considered for the formation of pyrite. Despite decades of research, determining the actual nature of the pyrite precursors and the mechanisms of pyrite formation in both abiotic and biotic experimental systems remains an important objective (Matamoros-Veloza *et al.*, 2018a; Matamoros-Veloza *et al.*, 2018b; Picard *et al.*, 2018).

The complexity of pyrite formation mechanisms and the difficulty to identify and characterize the intermediate species, especially at low temperature, explain the gap of knowledge that remains to be filled to understand the molecular-level mechanisms that govern the incorporation of elemental impurities in pyrite, especially when these elements are present at environmental trace levels. Nevertheless, better understanding the mineralogical properties of the precursors and their potential interactions with trace elements is essential to evaluate the ability of pyrite to serve as a trace element pump during early diagenesis and burial of sediments. Indeed, interactions at the solid-solution interface have a particular importance when considering pyrite as a scavenger for toxic elements in reducing sub-surface environments (Morse, 1994). Although kinetic effects on pyrite nucleation have already been shown for contents of metal or metalloid impurity in the percent range, little is known in the case of elemental impurities at trace levels that are more relevant to natural systems. Addressing this latter issue is however mandatory to further consider such kinetics effects on pyrite formation during early-diagenesis of marine and continental sediment.

Ni and As are among the most frequent trace elements in sedimentary pyrite, in which they exhibit the highest average concentrations among trace elements, within the hundreds to thousand ppm wt. range, locally reaching a few wt% (Gregory *et al.*, 2015). The objective of the present study was then to improve our understanding of the influence of these two trace elements on pyrite formation route and kinetics. To reach this goal, pyrite synthesis experiments were carried out at ambient temperature in presence of a thousand of ppm mol. of Ni(II) or As(III) in the starting solution. The mineralogical properties of the solid fractions were monitored over time by using synchrotron-based X-ray scattering and X-ray absorption spectroscopy analyses. We were thus able to determine precisely the evolution of the mineralogical sequence leading to pyrite formation and to further elucidate the mineralogical structure of the FeS precursor. In the three studied scenarios (*i.e.* a control synthesis aimed to form pure pyrite, Ni-doped synthesis and As-doped synthesis), our results revealed similar routes involving the same mineralogical pathway. However, our results also emphasized some different formation rates for pyrite, allowing us to draw hypotheses on Ni and As influence on pyrite nucleation mechanism.

MATERIALS AND METHODS

Pyrite syntheses at ambient temperature under anoxic conditions

Three pyrite synthesis experiments were performed at room temperature (25 ± 3 °C): a control batch referred to as “Fe-S”, meant to form pure pyrite and two batches containing either Ni(II) or As(III), meant to form Ni- and As-doped pyrite, respectively, and referred to as “Fe-S:Ni” and “Fe-S:As”. In these latter batches, the starting solutions contained Ni(II) or As(III) at a Ni:Fe or As:Fe molar ratio of 0.001. The synthesis protocol, adapted from previous studies by Wei and Osseo-Asare (1997) and Noël *et al.* (2014, 2015), was similar to that reported by Morin *et al.* (2017) for “Fe-S” and “Fe-S:Ni”, and by Le Pape *et al.*, (2017) for “Fe-S:As”, but with 10 and 5 times lower Ni:Fe and As:Fe molar ratios, respectively, in the present study (Table 1). Each synthesis glass vial was sealed with a butyl rubber stopper and maintained under vigorous stirring for 1510 hours (≈ 63 days) for the kinetic study and until 520 days to collect a final product.

Solids and solutions were sampled, and pH was measured, at specific time-steps (*i.e.* 0, 0.5, 40, 60, 114, 156, 204, 228, 252, 288, 324, 492, 758, 860, 1510 hours.) over the course of the experiments. The corresponding samples were referred to as Fe-S_*N*h, Fe-S:Ni_*N*h, and Fe-S:As_*N*h, for the three batch synthesis experiments, where *N*h stands for the sampling time after start. One last sampling occurred after 520 days to collect the final product of the experiment. The corresponding samples were referred to as Fe-S_520days, Fe-S:Ni_520days and Fe-S:As_520days. At each sampling time, solids were collected by centrifuging 3 to 12 mL of the suspension at 6000 rpm during 5 to 7 minutes, washed twice with O_2-free milli-Q water and vacuum-dried in an evacuator within the glove-box following previously approved protocols (Le Pape *et al.*, 2017; Morin *et al.*, 2017). Supernatants were filtered through 0.2 µm cellulose filters and stored for further elemental analysis. All these steps were carried out at ambient temperature.

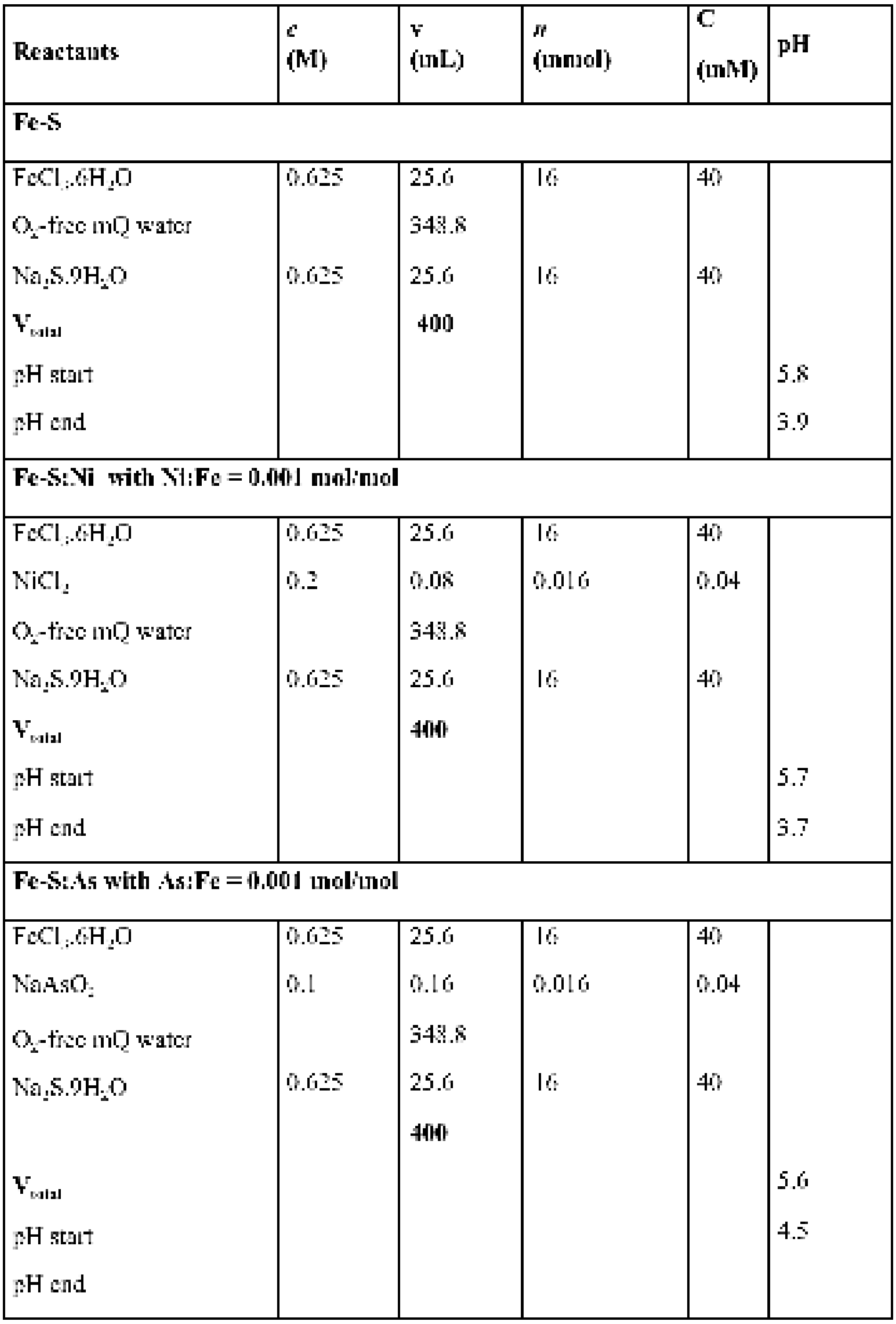

Reactants	***c*** **(M)**	**v (mL)**	***n*** **(mmol)**	**C (mM)**	**pH**
Fe-S					
$FeCl_3.6H_2O$	0.625	25.6	16	40	
O_2-free mQ water		348.8			
$Na_2S.9H_2O$	0.625	25.6	16	40	
V_{total}		**400**			
pH start					5.8
pH end					3.9
Fe-S:Ni with Ni:Fe = 0.001 mol/mol					
$FeCl_3.6H_2O$	0.625	25.6	16	40	
$NiCl_2$	0.2	0.08	0.016	0.04	
O_2-free mQ water		348.8			
$Na_2S.9H_2O$	0.625	25.6	16	40	
V_{total}		**400**			
pH start					5.7
pH end					3.7
Fe-S:As with As:Fe = 0.001 mol/mol					
$FeCl_3.6H_2O$	0.625	25.6	16	40	
$NaAsO_2$	0.1	0.16	0.016	0.04	
O_2-free mQ water		348.8			
$Na_2S.9H_2O$	0.625	25.6	16	40	
		400			
V_{total}					5.6
pH start					4.5
pH end					

Table 1. Synthesis protocol. Proportions of the reactants used for the Fe-S, Fe-S:Ni and Fe-S:As pyrite synthesis experiments. To prevent any atmospheric oxidation, the experiments were performed in an anoxic

Jacomex™ glove box (< 1 ppm O2) under a nitrogen atmosphere and using O2-free milli-Q water, degassed by bubbling N2 at 80°C for 45 min. Stock solutions were prepared from PROLABOTM salts in the glove box and were magnetically stirred for 72 hours before being used for the experiments. For the Fe-S synthesis experiment, 25.6 mL of the FeCl3 stock solution was mixed with 348.8 mL of O2-free milli-Q water under stirring. For the Fe-S-Ni and Fe-S-As doped experiments, appropriate volumes (v) of Ni or As stock solutions of concentration (c) were mixed with the 25.6 mL of the FeCl3 stock prior to water addition. Afterwards, the solution was completed with 25.6 mL of Na2S solution to reach 400 mL of total volume (Vtotal) in glass vials. These vials with initial concentrations of the reactants (C) were then sealed with butyl rubber stoppers and reacted at 25°C under constant stirring. Solution pH at the start and end of the synthesis experiments are also reported.

X-ray Absorption Spectroscopy at the Fe and S *K*-edges

Iron and sulfur speciation in the solid samples corresponding to each time step of the batch synthesis experiments were determined by using synchrotron-based X-Ray absorption spectroscopy at the Fe and S *K*-edges. Fe *K*-edge data were collected both in transmission and fluorescence detection modes at cryogenic temperature at 20 K in a liquid helium cryostat on the bending magnet SAMBA beamline at SOLEIL Synchrotron (Gif sur Yvette, France). The incoming beam energy was monitored by a Si(220) double-crystal monochromator equipped with sagittal focusing of the second crystal (Briois *et al.*, 2011). The incident beam energy was calibrated by measuring the Fe *K*-edge of a Fe(0) foil in double transmission mode and by setting its first inflection point to 7112 eV. Eleven to thirteen samples were analysed for each of the three synthesis experiments. The quantity of solid that could be obtained at each time step was of a few mg, which required the use of fluorescence detection for measuring most of the samples. The sample fluorescence signal was measured using a Canberra™ 36-elements Ge array detector. For these measurements, sample pellets were prepared by pressing a finely ground mixture of less than 1 mg of sample powder with 40 mg of cellulose, in a Jacomex™ glove box (O_2< 1 ppm). The pellets were covered with Kapton® tape and sealed in strictly anoxic containers that were transported to the synchrotron facility according to previously approved protocols (Morin *et al.*, 2017; Le Pape *et al.*, 2017). Samples were then mounted on the cryostat sample rod in a Jacomex™ glove box at SOLEIL and immersed in a liquid N_2 bath before being transferred into the beamline cryostat. Between 5 and 10 scans were necessary to obtain an acceptable signal-to-noise ratio depending on the analysed sample. Extended X-Ray Absorption Fine Structure (EXAFS) data at the Fe *K*-edge were averaged normalized, deglitched and background subtracted using the ATHENA software (Ravel and Newville, 2005).

Five samples from each batch synthesis experiments were further analysed at the S *K*-edge. X-ray Absorption Near-edge Structure (XANES) data were collected in fluorescence detection mode on beamline 4–3 at the Stanford Synchrotron Radiation Light Source (SSRL, California, United States of America). The energy of the incoming beam was monitored with a Si(111) double-crystal monochromator and the fluorescence signal was collected with a Hitachi™ HTA 4-element solid-state Si drift detector. Energy was calibrated by setting the energy position of the main edge of a thiosulfate reference at 2472 eV between each sample holder change during the experiment. A few mg of pure solid powders, shipped to SSRL within strictly anoxic containers, were spread over sulfur-free tape, mounted into sample holders in a COY™ glove box (H_2/N_2 atmosphere) onsite, and analysed at room-temperature in a sample chamber under He flow. Between 1 to 4 scans were collected for each sample. Data were calibrated and averaged using the SIXPACK software (Webb, 2005). Finally, averaged spectra were normalized using the ATHENA software (Ravel and Newville, 2005).

EXAFS and XANES data analysis

EXAFS data at the Fe *K*-edge were analysed via a Linear Combination Least Squares (LC-LS) fitting procedure using a custom-built software (Noël *et al.*, 2014; Morin *et al.*, 2017; Merrot *et al.*, 2019) based on the Levenberg-Marquardt minimization algorithm. Goodness of fit was estimated by a reduced chi-squares, $\chi^2_R = N_{ind} / [(N_{ind}-N_p)N_{points}\,\varepsilon^2] \sum [k^3\chi(k)_{exp} - k^3\chi(k)_{calc}]^2$, where $N_{ind} = (2\Delta k\Delta R)/\pi$ is the number of independent parameters, N_p is the number of fitting components, N_{points} the number of data points and ε is the measurement uncertainty. The ε value was estimated as the root mean square of the Fourier back-transform of the data in the 15-25 Å *R*-range (Ravel and Newville, 2005). Uncertainty on each fitting parameter *p* was estimated to 99.7% confidence (3 sigma) by $3[\mathrm{VAR}(p)\,\chi^2_R]^{½}$, where VAR(*p*) is the variance of parameter *p* returned by the minimization routine for the lowest χ^2_R. The EXAFS spectra of samples Fe-S_0.5h (just after start) and Fe-S_1510h (end) samples of the control batch (Fe-S) were the two only components used to fit the whole set of Fe *K*-edge EXAFS data. This procedure yielded a quantitative description of the onset of pyrite formation in the three batch synthesis experiments.

Shell-by-shell fitting of the Fe *K*-edge EXAFS spectra were also performed to analyse the local structure around Fe atoms in the solids collected over the course of the three batch synthesis experiments. The fitting was performed using theoretical phase-shift and amplitude backscattering functions generated from the crystal structure of mackinawite (Lennie *et al.*, 1995) using the FEFF8.1 code (Ankudinov *et al.*, 1998). Selected backscattering paths were used to fit the unfiltered k^3-weighted EXAFS spectra in *k*-space using the plane-wave formalism (Teo, 1986), with a custom-built least-squares fitting software (Maillot *et al.*, 2011; Maillot *et al.*, 2013) based on the Levenberg-Marquardt minimization algorithm. Fit quality and uncertainties on refined parameters were estimated using the same procedure as for the LC-LS fitting.

LC-LS fitting of the XANES spectra at S *K*-edge was performed using a custom-built program (Morin *et al.*, 2003) based on the Levenberg-Marquardt minimization algorithm. Fit quality was estimated by a R-factor, $Rf = \Sigma\, [\mu_{exp} - \mu_{calc}]^2 / \Sigma\, y_{exp}^2$, where μ is the normalized absorbance. It was also estimated by a reduced chi-squares already proposed by Stetten *et al.* (2018) and Seder-Colomina *et al.*, (2018), $\chi^2_R = N_{ind} / (N_{ind}-N_p) \sum [\mu_{exp} - \mu_{calc}]^2$, where N_p is the number of fitting components and N_{ind} is the number of independent parameters corresponding to the energy range divided by the natural width of the Fe *K*-level reported by Krause and Oliver (1979). The uncertainty on the fitting components was estimated using the same procedure as for EXAFS fitting.

For LC-LS fitting of S *K*-edge XANES data, the set of model compound included mackinawite (FeS), elemental sulfur (S(0)) and synthetic pyrite (FeS_2). FeS refers to a biogenic mackinawite synthesized by incubating *Desulfovibrio capillatus* with Fe(III)-citrate during 1.5 months, designated as "bio-FeS 1.5 month" in Ikogou *et al.* (2017). Extensive mineralogical characterization of this sample by Ikogou *et al.* (2017) indicates that it consists of nano-mackinawite. A powder sample of alpha-sulfur S(0) was taken from the IMPMC chemical stocks, and FeS_2 was pure pyrite synthesized according to the protocol reported by (Morin *et al.*, 2017). As self-absorption was observed for the S(0) sample, the XANES spectrum was corrected using the ATHENA software to match the spectrum collected in transmission mode reported in (Phan *et al.*, 2019). The S *K*-edge XANES spectra of these references are shown in SI (Fig. SI-4).

Powder X-Ray Diffraction (XRD) and Wide Angle X-ray scattering – Pair distribution function (WAXS-PDF) data collection and analysis

Powder XRD patterns of the final samples taken at 1510 hours and 520 days were collected in Debye-Scherrer configuration using a Mo Kα rotating anode as detailed in Fig. SI-2.

Powder XRD-WAXS pattern of the Fe-S_0.5h sample was collected at 24 keV (0.5141 Å) in Debye-Scherrer geometry up to $2\theta = 125°$ ($Q_{max} = 4\pi\sin\theta_{max})/\lambda = 21.7$ A^{-1}) on the 2-circle diffractometer of the CRISTAL beamline (SOLEIL synchrotron) equipped with a MYTHEN2 X 9K detector (DECTRIS). Finely ground powder was put in a borosilicate capillary and sealed in a glove box using a cyanoacrylate-based glue. Data were collected for 1 hour using a 2θ step of 0.004° and the background from the borosilicate capillary was subtracted prior to data analysis.

Rietveld analysis of the Fe-S_0.5h sample XRD pattern was performed over the 2-100° 2θ range with the xnd_1.3 code (Berar and Baldinozzi, 1998) using pseudo-Voigt line-shape profiles. The space groups, atomic positions and isotropic Debye-Waller factors were taken from Rettig and Trotter (1987) and Lennie *et al*. (1995) for α-elemental sulfur S(0) and mackinawite FeS structures, respectively. Anisotropic crystallite shape and size as well as isotropic strain effects were refined by combining Lorentzian and Gaussian line-shape functions, respectively. No preferential orientation parameters were used. The scale factors retrieved from the Rietveld analysis were used to calculate relative weight fraction of the mineral phases in the sample. Line widths were used to calculate the mean coherent domain (MCD) size from the Scherrer equation. In the case of mackinawite, which is a platelet-type mineral, an anisotropic MCD shape was used.

PDF analysis was performed from the Fe-S_0.5h sample WAXS data. The PDF G(r) gives the probability of finding a pair of atoms separated by a distance *r*. It is experimentally obtained from the sine Fourier transform of the scattering function S(Q) (Egami and Billinge, 2003; Farrow and Billinge, 2009) as shown in the following equation :

$$G(r) = \frac{2}{\pi}\int_{Q_{\min}}^{\infty} Q[S(Q) - 1]\sin Qr\, \mathrm{d}Q$$

PDFgetX3 (Farrow *et al.*, 2007) was used to process the experimental powder diffraction intensity to generate the G(r). For each sample, the experimental G(r) was fitted with a one calculated from a crystal structure model using the PDFgui program (Farrow *et al.*, 2007), similar to a Rietveld refinement albeit performed in the direct space. Only scale factor, followed by unit cell parameters and atomic displacement parameters were refined. Gaussian resolution dampening factor (Qdamp = 0.0039) was refined from a LaB6 pattern measured in the same conditions. Spherical coherent domains were assumed for the Fe-S_0.5h sample and a sp diameter factor was adjusted to match the signal dampening of the PDF in the nanoparticle structure. The agreement between the calculated and the experimental PDF is characterized by the following reliability factor:

$$R_{\mathrm{w}} = \sqrt{\frac{\sum_{i=1}^{N} \left[G_{\mathrm{obs}}(r_i) - G_{\mathrm{calc}}(r_i; \vec{\mathbf{p}})\right]^2}{\sum_{i=1}^{N} G_{\mathrm{obs}}{}^2(r_i)}}$$

where G_{obs} is the PDF extracted from the diffraction data, G_{calc} is the PDF calculated from the model and p is the list of parameters refined in the model.

Scanning Electron Microscopy coupled with Energy Dispersive X-ray Spectroscopy (SEM-EDXS)

SEM-EDX data were collected at IMPMC, with a GEMINI ZEISS™ Ultra55 Field Emission Gun Scanning Electron Microscope equipped with a Bruker™ Si-drift detector for EDXS. Prior to analysis, samples were deposited as ground powder on carbon tape in an anoxic glovebox.

RESULTS

Kinetic of pyrite formation in the presence or absence of Ni or As

According to observations from previous pyrite synthesis experiments at room temperature (Noël *et al.*, 2015; Morin *et al.*, 2017; Le Pape *et al.*, 2017), a change in colour of the batch suspension can be used to reveal the onset of pyrite formation. Indeed, the matt black colour of the suspension at the beginning of the experiment turns progressively to an anthracite grey colour when the FeS precursors convert to pyrite. In addition, the density and rate of flocculation of the particles changes drastically as they evolve from FeS to pyrite. When agitation is interrupted for a few minutes, particles tend to settle much faster in the presence of pyrite than in the presence of FeS. Moreover, the volume of nanoparticles accumulated at the base of the bottle seems much more compacted in the presence of pyrite: the initial volume of material seems to decrease by 2 to 3 times when the particles go from FeS to pyrite. In the present study, such a colour and volume change was observed after 5 days for Fe-S:Ni, 14 days for Fe-S and 32 days for Fe-S:As. These trends suggest that pyrite formed more rapidly in the presence of Ni and more slowly in the presence of As.

This difference in pyrite formation kinetics is further demonstrated by Fe *K*-edge EXAFS spectroscopy analysis of the solid samples formed over the course of the batch synthesis experiments, as detailed hereafter. The unfiltered k^3-weighted Fe *K*-edge EXAFS spectra of the solids sampled over time in the Fe-S, Fe-S:Ni and Fe-S:As batch synthesis experiments are displayed in Figure 1, together with their corresponding Fast Fourier Transforms (FFT). These EXAFS data provide a time-course evolution of the local structure around Fe atoms in each of the three synthesis conditions (*i.e.* as a function of the presence or absence of Ni or As) and reveal the kinetics of pyrite formation in each case. The EXAFS spectra of all samples from the three batch synthesis experiments could be fitted with the spectra of the Fe-S_0.5h and Fe-S_1510h samples as sole LC-LS fitting components (Fig. 1 and Table 2). This result indicates that Fe speciation over the course of our experiments can be represented as a combination of Fe speciation in the starting and end products. The starting product, represented by sample Fe-S_0.5h, contains Fe mostly in the form of poorly ordered FeS. Its Fe *K*-edge EXAFS spectrum is similar to that of starting samples in the pyrite synthesis reported by Morin *et al*. (2017). The end product, represented by sample Fe-S_1510h, consists of micro-crystalline pyrite. Its Fe *K*-edge EXAFS spectrum is similar to that obtained by Morin *et al*. (2017) and Le Pape *et al*. (2017) from comparable syntheses (Fig. SI-3). XRD analysis confirmed that the Fe-S_1510h, Fe-S:Ni_1510h and Fe-S:As_1510h samples consisted of pyrite with trace amounts of α-sulfur and NaCl (Fig. SI-2). The same XRD pattern for pyrite is obtained for the samples collected after 520 days (Fig. SI-2), indicating that the crystallite size of pyrite did not significantly evolve after 1510h. The crystal shape and texture of the pyrite end product, as observed by SEM in the 520 days samples, was comparable for the three syntheses experiments (Fig. 2). The submicron pyrite particles, approaching a cuboctahedral habitus, consist of aggregates of nanosized platelets, as previously observed by Le Pape *et al.* (2017). SEM-EDX spectra (Fig. 2) and bulk XRF spectra (Fig. SI-6) indicated the presence of trace amounts of Ni or As in the Fe-S:Ni and Fe-S:As pyrite end products, respectively. This result is consistent with the incorporation of Ni or As in the pyrite structure in previous comparable synthesis experiments, as detailed by Morin *et al.* (2017) and Le Pape *et al.* (2017). According to the initial Ni:Fe and As:Fe molar ratio of 0.001 reported in Table 1, and assuming similar solid-liquid partition as those observed by Morin *et al.* (2017) and Le Pape *et al.* (2017), the molar fraction of Ni and As in the pyrite end product is estimated to 0.2 mol%, since half the initial Fe remains as aqueous Fe^{2+}.

Pyrite began to be observed in statistically significant proportions after 324 hours (11±2% at 14 days) in the Fe-S control experiment, and was the dominant Fe species after 492 hours (76±5% at 21 days) (Fig. 1, Table 2). The occurrence of pyrite is typically visible in the FFT of the Fe *K-edge* EXAFS data, where the peak at $R+\Delta R = 3.6$ Å (uncorrected for phase-shift) is due to Fe-Fe paths at 3.82 Å (Morin *et al.*, 2017). In the Fe-S:Ni experiment, pyrite formed faster since it could be detected after 114 hours (16±1% at 5 days) and it was found as the major Fe species after 204 hours (70±1% at 8.5 days and 88±4% at 9.5 days) (Table 2). It was found to constitute more than 85% of the final product at 1510 hours (63 days) (Table 2). In spite of this accelerated pyrite formation, a remaining proportion

(≤ 20%) of FeS was however observed after 492h and it could also be present after 1510 hours, given the uncertainty in the fitting of this latter sample spectrum (Table 2, Fig. 1). In contrast, pyrite formation was slow in the Fe-S:As experiment, with a first pyrite occurrence detected after 758 hours (48±1% at 32 days) and a fraction of 90±1% pyrite after 860 hours (36 days). In this experiment, the onset of pyrite formation occurred between 492 and 758 hours, since no pyrite was detected in the 492h sample (Fig. 1, Table 2).

As shown by the LC-LS fitting results detailed above (Fig. 1, Table 2), the Fe *K*-edge EXAFS spectrum of the Fe-S_0.5h sample matches that of the poorly-ordered FeS model compound in all the three batch experiments. This result suggests that the FeS precursors are similar in the three batch synthesis experiments. In addition, the similarity of the Fe *K-edge* EXAFS spectra of the final samples indicates that the final product is the same in the three batch synthesis experiments (Fig. 1).

Finally, pyrite formed 2.4 times faster than in the control in the presence of Ni, whereas it formed 1.5 times slower than in the control in the presence of As. These results indicate that Ni accelerated pyrite precipitation while As decelerated it, though these impurities were present at trace level (Ni:Fe = As:Fe = 0.001 mol/mol) in the initial solutions.

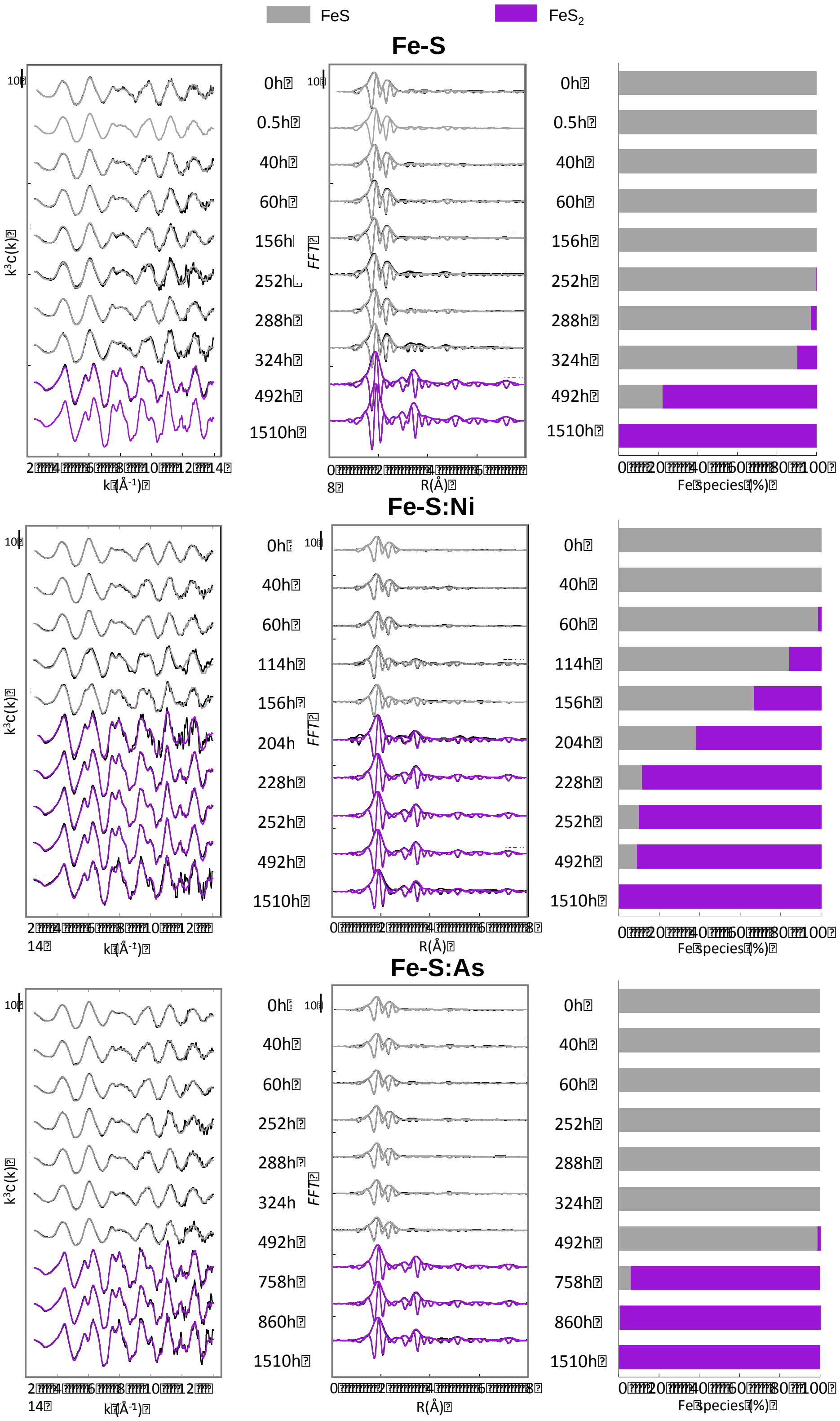

Figure 1. Time-course analysis of Fe speciation in the three pyrite synthesis experiments (Fe:S; Fe:S-Ni; Fe-S:As), as determined by LC-LS fitting of Fe *K*-edge data. From left to right, Fe *K*-edge k^3-weighted EXAFS spectra, corresponding Fast Fourier transforms and normalized results of LC-LS fitting analysis showing the percentage of each Fe species occurring over time. Experimental data are displayed in black. LC-LS fits are shown in grey and purple, respectively for FeS and FeS_2, depending on the dominant compound in the sample. FeS is represented by the spectrum of the sample Fe-S_0.5h and FeS_2 is represented by the sample Fe-S_1510h. Results, uncertainties and fit quality are listed in Table 2.

Sample	**FeS (%)**	**FeS_2 (%)**	**Sum**	**c^2_R**	***R*-factor**
Fe-S_0h	94(4)	0(3)	94	0.527	0.046
Fe-S_0.5h	100		100		
Fe-S_40h	99(5)	0(3)	99	0.722	0.025
Fe-S_60h	100(0)	0(2)	100	1.093	0.037
Fe-S_156h	100(0)	0(0)	100	1.368	0.034
Fe-S_204h	100(1)	0(0)	100	1.227	0.032
Fe-S_252h	100(0)	0(3)	100	1.550	0.097
Fe-S_288h	100(0)	3(2)	103	0.963	0.021
Fe-S_324h	100(0)	11(2)	111	0.918	0.077
Fe-S_492h	22(9)	76(5)	98	2.173	0.013
Fe-S_1510h		100	100		
Fe-S:Ni_0h	96(1)	1(5)	96	1.979	0.016
Fe-S:Ni_40h	100(4)	0(0)	100	0.639	0.029
Fe-S:Ni_60h	99(6)	2(1)	101	1.465	0.018
Fe-S:Ni_114h	87(13)	16(1)	104	6.240	0.089
Fe-S:Ni_156h	64(1)	32(4)	96	1.167	0.029
Fe-S:Ni_204h	44(7)	70(1)	114	0.949	0.139
Fe-S:Ni_228h	11(4)	88(4)	99	2.487	0.013
Fe-S:Ni_252h	10(3)	88(11)	98	11.312	0.014
Fe-S:Ni_492h	9(19)	89(1)	98	9.129	0.014
Fe-S:Ni_1510h	0(16)	86(2)	86	0.529	0.113
Fe-S:As_0h	95(5)	0(0)	95	1.364	0.016
Fe-S:As_40h	96(0)	0(0)	96	0.545	0.031
Fe-S:As_60h	95(1)	0(0)	95	1.321	0.020
Fe-S:As_252h	99(0)	1(3)	101	1.514	0.049
Fe-S:As_288h	100(5)	0(0)	100	0.827	0.028
Fe-S:As_324h	99(7)	0(0)	99	1.631	0.024
Fe-S:As_492h	93(1)	1(2)	94	0.668	0.042
Fe-S:As_758h	6(6)	86(2)	91	0.611	0.021
Fe-S:As_860h	1(5)	90(1)	90	0.528	0.027
Fe-S:As_1510h	0(8)	92(8)	92	0.701	0.051

Table 2. Results of LC-LS fitting analysis of Fe *K*-edge EXAFS spectra of solid samples collected over the course of the Fe-S, Fe-S:Ni and Fe-S:As synthesis batch experiments. All spectra were least-squares fit using two components: i) the spectrum of the FeS precursor of pyrite in our experiments that corresponds to Fe_xS_x nano-clusters in mixture with poorly ordered mackinawite (see text), represented by sample Fe-S_0.5h (in grey in the table) and ii) the spectrum of pure pyrite, FeS_2 (see text) represented by sample Fe-S_1510h (in purple in the table). Fit quality is estimated by a reduced chi-squares χ^2_R and a R-factor (see text). Uncertainties on the reported values are reported for the last digit under bracket, with 99.7% confidence interval (see text).

Evolution of solid-state speciation of sulfur over the course of pyrite synthesis

Solid samples from five main stages of each batch synthesis experiment were further analysed using XANES spectroscopy at the S *K*-edge: the start of the synthesis (t = 0 hr), three time steps encircling pyrite formation and the final sample (t = 1510 hr). Figure 3 shows the time course of the S *K*-edge XANES spectra for the three batch synthesis experiments Fe-S, Fe-S:Ni and Fe-S:As. As suggested by XRD analyses reported by Morin *et al.*, (2017) and Le Pape *et al.* (2017) for comparable synthesis experiments, nanocrystalline mackinawite (FeS), elemental sulfur (S(0)) and pyrite (FeS_2) were considered as the most relevant model compounds for representing S speciation in the samples (Fig. SI-4). These model compounds indeed gave the best LC-LS fits of the experimental S *K*-edge XANES spectra (Fig. 3, Table 3). Fitting results show that FeS and S(0) formed first in the three batch synthesis experiments and transformed to FeS_2 with time. By the end of the experiment, the Fe-S_1510h, Fe-S:Ni_1510h and Fe-S:As_1510h samples contained 88±7%, 77±4% and 95±3% of S as FeS_2, respectively. No FeS was found in the Fe-S_1510h and Fe-S:As_1510h samples, whereas 21±2% of S remained as FeS in the Fe-S:Ni 1510h sample. In this latter sample, only 2±3% of elemental sulfur was detected, which indicated that, if present, it was below the typical detection limit of XANES analysis (<5%) (Morin *et al.*, 2003). Elemental sulfur accounts for 10±4% and 6±3% in the Fe-S_1510h and Fe-S:As_1510h samples (Table 3). These results are in agreement with XRD analysis performed in the final samples which confirmed they mainly consist of pyrite with residual traces of S(0)(Fig. SI-2). FeS was not detected by XRD in these samples likely because of its nanosized/amorphous character and low amount.

The LC-LS fitting of the S *K*-edge XANES data (Fig. 3, Table 3) indicated the occurrence of pyrite at similar time steps than Fe *K*-edge EXAFS data (Fig. 1, Table 2). In the Fe-S control synthesis experiment, pyrite appeared after 324 hours (20±15% of total S) and it was found as the major S species after 492 hours (82±3%) (Fig. 3, Table 3). In the Fe-S:Ni batch synthesis experiment, pyrite was observed in significant amounts after 114 hours (29±3%) and it was found as the major S species after 228 hours (52±6%). In the As-bearing batch synthesis experiment, pyrite was detected as the major S species after 758 hours (88±3 %) (Fig. 3, Table 3).

These results back up the Fe *K*-edge EXAFS analysis and confirm that the kinetic of pyrite formation significantly depends on the presence of Ni and As at trace levels. Overall, although pyrite is observed much earlier in the batch with Ni, the experiments performed without Ni seem to produce larger quantities of pyrite (i.e., 88±7% and 95±3% after 1510 hours in the Fe-S and Fe-S:As systems, respectively, compared to 80% in the Fe-S:Ni system). The experiments with As appear to be more efficient because after 758 hours, the major S species of the solids are only composed of S(0) and pyrite (95±3%) and there is no more FeS remaining (Table 3). In addition, S *K*-edge XANES analysis of S speciation reveals that both elemental sulfur S(0) and FeS progressively disappear at the expense of pyrite in the three batch synthesis experiments. This latter result suggests that both elemental sulfur S(0) and FeS are primary solid precursors for pyrite in presence or absence of Ni or As trace impurities. Interestingly, LC-LS fitting results of S *K*-edge XANES data indicate that no major component is lacking to reconstruct the experimental spectra. This latter point suggests that the only S species occurring in our synthesis experiments were elemental sulfur S(0), FeS and pyrite (FeS_2). However, regarding its intermediate energy position between those of S(-I) and S(0), the S *K*-edge for polysulfide S_n^{2-} anions might be matched by a combination of pyrite and α-sulfur fitting components. Considering their possible contribution to pyrite formation (Rickard and Luther, 2007), the occurrence of polysulfides in our samples containing both α-sulfur and H_2S cannot be ruled out.

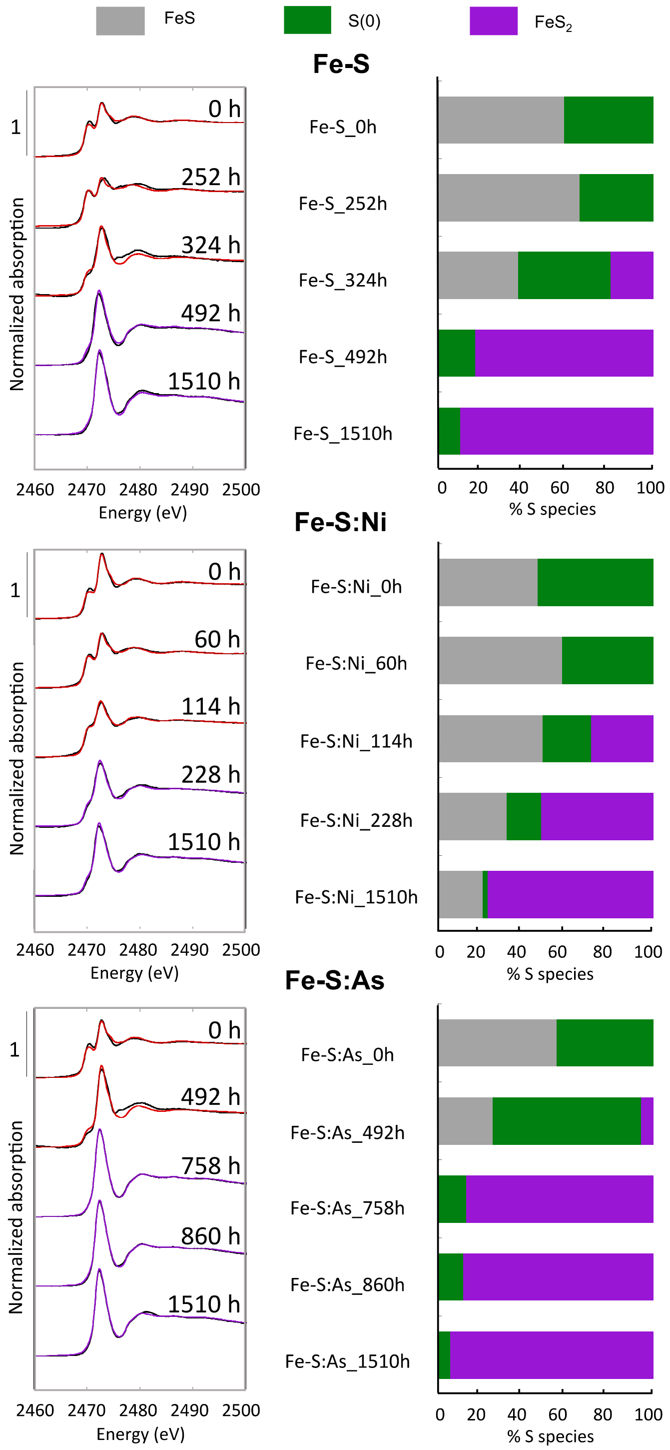

Figure 3. Time-course analysis of S speciation in the three synthesis experiments, as determined by LC-LS fitting analysis of S *K*-edge XANES data (Table 3). The three fitting components are: FeS, S(0) and FeS_2 with corresponding spectra reported in Figure SI-4. Normalized percentages of each fitting component are displayed on the right panel. Experimental spectra are displayed in black. LC-LS fits are shown in red for the pyrite precursors (FeS and/or S(0)) and in purple for FeS_2. Results, uncertainties and fit quality are listed in Table 3.

Sample	FeS (%)	S(0) (%)	FeS_2 (%)	Sum	Chi^2_R	*R*-factor
Fe-S_0h	59(1)	41(1)	0(0)	100	0.002	0.0003
Fe-S_252h	67(2)	35(2)	0(0)	101	0.005	0.0010
Fe-S_324h	39(7)	45(14)	20(15)	104	0.022	0.0039
Fe-S_492h	0(0)	17(3)	82(3)	99	0.002	0.0003
Fe-S_1510h	0(5)	10(4)	88(7)	101	0.004	0.0007
Fe-S:Ni_0h	46(1)	54(1)	0(0)	100	0.002	0.0004
Fe-S:Ni_60h	58(2)	42(2)	0(0)	100	0.022	0.0039
Fe-S:Ni_114h	49(1)	23(3)	29(3)	100	0.001	0.0003
Fe-S:Ni_228h	32(4)	16(6)	52(6)	100	0.003	0.0005
Fe-S:Ni_1510h	21(2)	2(3)	77(4)	100	0.002	0.0005
Fe-S:As_0h	55(1)	45(1)	0(0)	100	0.002	0.0004
Fe-S:As_492h	26(8)	70(17)	6(17)	101	0.022	0.0039
Fe-S:As_758h	0(2)	13(2)	88(2)	102	0.000	0.0001
Fe-S:As_860h	0(1)	11(2)	88(3)	100	0.001	0.0002
Fe-S:As_1510h	0(0)	6(3)	95(3)	101	0.002	0.0003

Table 3. Results of LC-LS fitting analysis of S *K*-edge XANES spectra of the five chosen solid samples collected over the course of the Fe-S, Fe-S:Ni and Fe-S:As synthesis batch experiments. All spectra were least-squares fit using three components (see text and Figure SI-4): (i) FeS, (ii) elemental sulfur S(0) and (iii) pyrite FeS_2. Fit quality is estimated by a reduced chi-squares χ^2_R and a R-factor (see text). Uncertainties on the reported values are reported for the last digit under bracket, with 99.7% confidence interval (see text).

Mineralogy of the FeS precursors of pyrite

To better understand in which way the presence of trace amounts of Ni and As has influenced pyrite formation kinetics, we have determined the mineralogical characteristics of the FeS precursors of pyrite in our batch synthesis experiments. Shell-by-shell analysis of the Fe *K*-edge EXAFS spectra were carried out on the samples collected before the apparition of pyrite. These analyses indicated that the local structure of the FeS precursors to pyrite was identical in the three batches and did not vary significantly over the course of the synthesis experiments (Table SI-2), being similar to that in the Fe-S_0.5h sample (Fig. 4C, Table 5, Table SI-2). The short-range crystal structure of these FeS precursors to pyrite was further investigated using synchrotron-based XRD (Fig. 4A, Table 4) and WAXS-PDF (Fig. 4B, Table 4) in addition to Fe *K-edge* EXAFS data.

Rietveld analysis of the synchrotron-based XRD powder pattern of the Fe-S_0.5h sample (Fig. 4A) indicated that it contains two crystalline components: 78±1% of FeS and 22±1% of S(0). These results are in agreement with the results of S *K*-edge XANES analysis. The crystallographic parameters and mean crystallite sizes of the identified phases are reported in Table 4, in which they are compared with the crystal structures of S(0) (Rettig and Trotter 1987) and mackinawite (Lennie *et al*. 1995). The unit cell parameters of the S(0) compound observed in our experiment are consistent with those of α-sulfur (Rettig and Trotter 1987) (Fig. 4A, Table 4). In contrast, the structure of the FeS species that was identified in our experiments does not perfectly match that of crystalline mackinawite (Lennie *et al*. 1995). Indeed, the refined unit-cell parameters of the FeS phase in our sample (*a* = 3.70±0.02 Å and *c* = 5.24±0.07 Å; Table 4) are slightly larger than those of crystalline mackinawite (3.6735±0.0004 Å and 5.0328±0.0007 Å; Lennie *et al*. 1995; Table 4). In addition, since the Mean Coherent Domain

(MCD) size of our FeS phase was as small as MCD*c* = 21±1 Å and MCD*ab* = 41±2 Å, we interpret this phase as nano-mackinawite, referred to as $FeS_{(nanoMck)}$ hereafter. In this phase, the Fe-S and Fe-Fe distances are both longer than those in crystalline mackinawite, with the first S neighbouring atom at 2.29±0.02 Å and the first Fe neighbour at 2.61±0.02 Å instead of 2.2558±9 Å and 2.5976±3 Å as reported by Lennie *et al.* (1995), respectively (Table 4). This longer distance and the small MCD measured for this FeS phase in our Fe-S_0.5h sample is consistent with the observed characteristics of nano-mackinawite or "freshly precipitated" mackinawite previously reported in the literature (Wolthers *et al.*, 2003; Ohfuji and Rickard, 2006; Jeong *et al.*, 2008). These previous studies emphasized the longer lattice spacings of their synthetic mackinawite compared to the crystalline mackinawite analysed by Lennie *et al.* (1995). According to Wolthers *et al.* (2003), this unit-cell expansion was ascribed to lattice relaxation due to decreasing crystallite size and to possible intercalation of water molecules.

Further analysis of the Fe-S_0.5h sample using WAXS-PDF yielded additional information on its mineralogical composition. As a matter of fact, two populations of FeS phases were necessary to reconstruct with the highest detail the distances of the first pairs of atoms in the PDF of the sample (Fig. 4B, Table 4). However, refinement of the Fe-S_0.5h sample PDF data did not require to include S(0) as a mineral component, likely because the S-S pair scattering contribution to the PDF is lower than that of Fe-S and Fe-Fe pairs from the dominant FeS phases (78±1 wt%). The two FeS phases used for the PDF refinement of the Fe-S_0.5h sample could be distinguished by their MCD sizes and their crystallographic parameters (Table 4). The first one was a nanocrystalline FeS phase with refined crystallographic parameters close to those of the $FeS_{(nanoMck)}$ phase identified by Rietveld analysis. Assuming isotropic MCD shape, PDF analysis indicated a MCD_{iso} of 27.7±9.6 Å for this phase (*i.e.* lower but in the same range than that determined by Rietveld analysis MCD_{ab}= 41±2 Å and MCD_c= 21±2 Å). The second FeS phase, with slightly different crystallographic parameters, required to be fit with even smaller particle size (*i.e.* MCD_{iso} size of 8±4 Å) and is further designated as $FeS_{(cluster)}$ in agreement with the predicted characters reported for this type of clusters by Rickard and Morse (2005). This latter MCD size for $FeS_{(cluster)}$ is comparable with the short range order < 7 Å reported by Csákberényi-Malasics *et al.* (2012) for FeS precipitated from $FeSO_4$ and C_2H_5NS mixing solutions. In a more recent study, Matamoros-Veloza *et al.* (2018b) reported FeS_{Nano} precipitates of 0.46±0.01 nm. In the present study, PDF fitting results indicate that the $FeS_{(cluster)}$ phase accounts for 53 wt% of the total FeS in the Fe-S_0.5h sample, while $FeS_{(nanoMck)}$ accounts for 47 wt% (Table 4). These respective fractions of both phases suggest that partial aggregation and crystallisation of FeS precursors has already occurred only 30 minutes after Fe(III) and H_2S mixing. The Fe-S distances determined by PDF analysis for $FeS_{(nanoMck)}$ and $FeS_{(cluster)}$ are 2.29±0.05 Å and 2.19±0.05 Å, respectively (Table 4**)**. Mixture of both phases yields a peak at 2.25 Å in the PDF (Fig. 4B). The Fe-Fe distance in $FeS_{(nanoMck)}$ and $FeS_{(cluster)}$ are 2.61±0.04 Å and 2.70±0.05 Å, respectively (Table 4). This short Fe-S bond length observed for the $FeS_{(cluster)}$ component is close to that reported by Rickard and Morse (2005) for Fe_2S_2

and Fe_4S_4 (*i.e.* 2.20 and 2.22 Å, respectively). In this latter study, the Fe-Fe distance estimated for these two Fe_xS_x (*i.e.* 2.83 and 2.80 Å, respectively) is also clearly higher than the one of mackinawite, which is also the case for our $FeS_{(cluster)}$.

Shell-by-shell fitting of the Fe *K*-edge EXAFS data was performed to give additional information on the local structure around Fe in the Fe-S_0.5h sample. Best fits were obtained with 3.0±0.1 S at 2.251±0.002 Å as first neighbour atoms and 1.7±0.2 Fe at 2.675±0.002 Å as second neighbour atoms (Fig. 4C, Table 5). These Fe-S and Fe-Fe distances are consistent with those obtained from XRD and PDF data. Indeed, each of these distances matches the average of the corresponding distances in $FeS_{(nanoMck)}$ and $FeS_{(cluster)}$ (Tables 4 and 5). The lower number of Fe second neighbours atoms compared to that expected for theoretical crystalline mackinawite (*i.e.* N = 4; Table 5, Lennie *et al.* (1995)) confirms that the FeS precursors in the Fe-S_0.5h sample are nanosized. Indeed, for small particle sizes a considerable dampening of the EXAFS signal is expected, as observed for instance for nano-Fe (oxyhydr)oxides by Maillot *et al.* (2011). Additionally, this lack of second neighbour contribution could also be attributed to vacancies within the FeS structure due to substituting Fe(III) (Bourdoiseau *et al.*, 2011). Indeed, our experiment starts with Fe(III) in solution, which could lead to the incorporation of small amounts of unreacted Fe(III) in FeS during its initial stage of formation, concomitantly to Fe(III) reduction by H_2S. Another notable result is the low number of neighbours found around 3.67 Å, corresponding to the theoretical positions of Fe atoms located at the corner of the *ab* plane. The lower number of Fe and of S neighbour atoms at 3.67 Å and 4.31 Å respectively compared to theoretical crystalline mackinawite could be due to a mixture of both $FeS_{(nanoMck)}$ and $FeS_{(cluster)}$ phases.

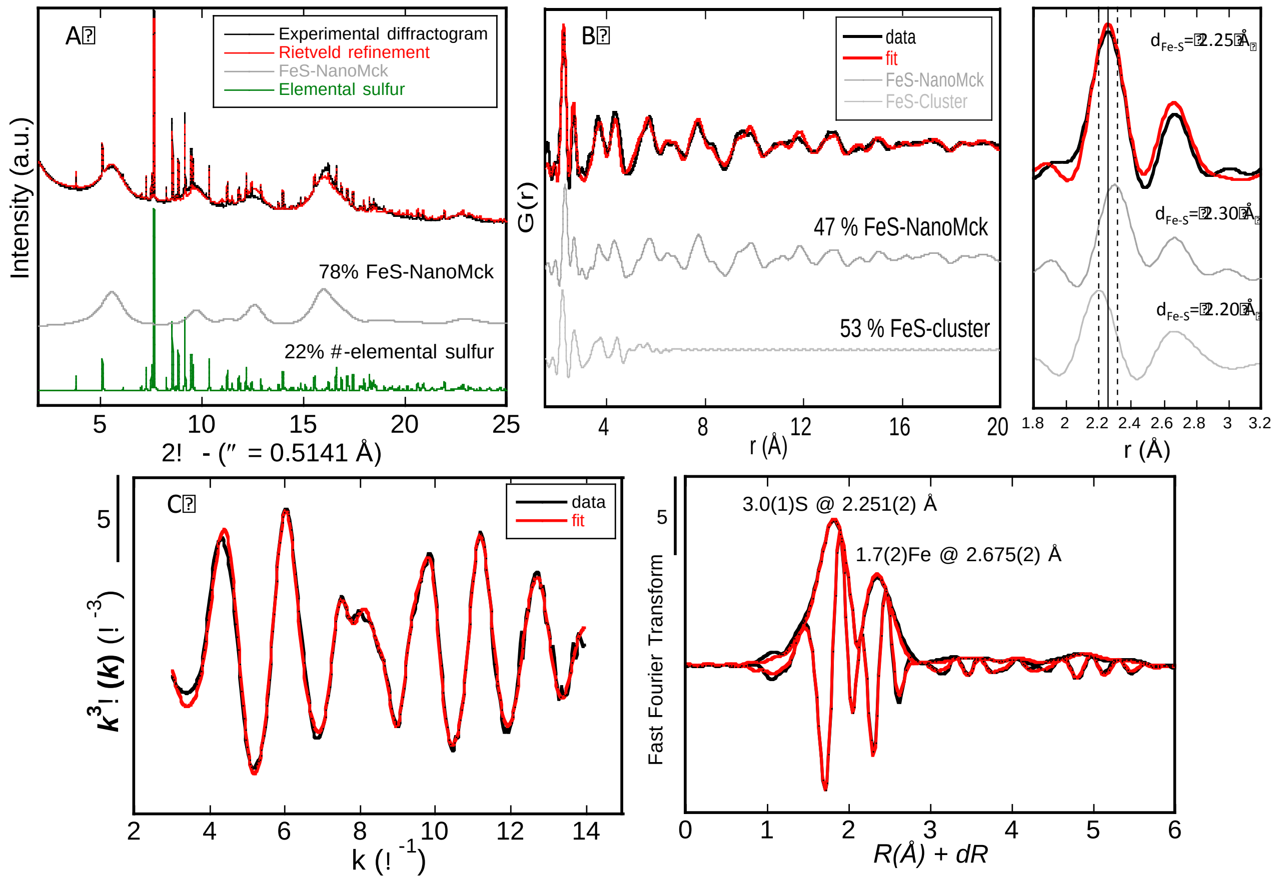

Figure 4. Detailed mineralogical analysis of the sample **Fe-S_0.5h**. Experimental and calculated curves are plotted in black and red colours, respectively. **A.** Rietveld refinement of the powder X-Ray diffraction pattern. The mineralogical phases observed are nanocrystalline mackinawite (78%) and α-elemental sulfur (22%); refined crystallographic parameters are reported in Table 4. **B.** Pair Distribution Function (PDF) analysis. The best-fit solution is obtained from the refinement in real space of two FeS populations with different coherent size domains: FeS-NanoMck (47%) and FeS-cluster (53%). Refined parameters are reported in Table 4. **C.** Results of the shell-by-shell fitting procedure applied to the Fe *K*-edge k^3-weighted EXAFS spectrum over the 3-14 k-range using phase-shift and amplitude functions simulated using the ab initio Feff8.1 code (Ikogou *et al.*, 2017). Fitting parameters are given in Table 4 and compared to the theoretical parameters of crystalline mackinawite (Lennie *et al.*, 1995). Fitting parameters of the shell-by-shell fitting procedure are listed in Table 5.

	a	*b*	*c*	*MCD$_{ab}$* *(Å)*	*MCD$_c$* *(Å)*	*MCDiso* *(Å)*	*R$_{wp}$* *(%)*	*dFe-S*	*dFe-Fe*
α-sulfur *(Rettig and Trotter 1987)*	10.4646(1)	12.8660(1)	24.4860(3)						
α-sulfur (22±1 wt%) this study	10.449(4)	12.849(5)	24.450(9)						
Mackinawite *(Lennie et al. 1995)*	3.6735(4)		5.0328(7)					2.2558(9)	2.5976(3)
FeS-NanoMck (78±1 wt%) this study	3.70(2)		5.24(7)	41(2)	21(1)		7.8	2.29(2)	2.61(2)
FeS-NanoMck (47 mol%) this study	3.70(5)		5.2(2)			27.7(9.6)		2.29(5)	2.61(4)
FeS-Cluster (53 mol%) this study	3.82(6)		4.1 (2)			8.4(4.3)	0.33	2.19(5)	2.70(5)
Fe_S_0.5h This study								2.251(2)	2.675(2)

Table 4. Comparison of the crystallographic parameters of the mineralogical phases identified from XRD-Rietveld, WAXS-PDF, and EXAFS Fe K-edge analyses of Fe-S_0.5h (Figure 4). Crystalline phases determined by XRD-Rietveld were alpha-sulfur (22 wt%) and nanocrystalline mackinawite (78%, hereafter designed as FeS-NanoMck). MCD is the abbreviation for Mean Coherent Domain. Refined parameters obtained for the PDF calculation using the mackinawite (Lennie et al., 1995) structure as starting model included two components: FeS-NanoMck (47 mol%) and FeS-cluster (53 mol%). Distances of first neighbours Fe-S and Fe-Fe are reported and compared as derived from each technique of measurement. Uncertainties in the refined parameters given in brackets refer to the last digit.

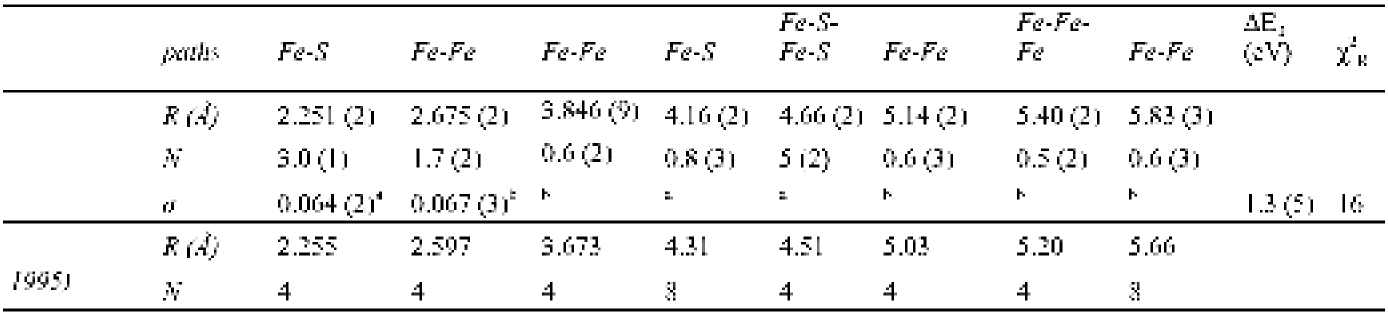

	paths	*Fe-S*	*Fe-Fe*	*Fe-Fe*	*Fe-S*	*Fe-S-Fe-S*	*Fe-Fe*	*Fe-Fe-Fe*	*Fe-Fe*	ΔE$_0$ (eV)	χ^2_R
	R (Å)	2.251 (2)	2.675 (2)	3.846 (9)	4.16 (2)	4.66 (2)	5.14 (2)	5.40 (2)	5.83 (3)		
	N	3.0 (1)	1.7 (2)	0.6 (2)	0.8 (3)	5 (2)	0.6 (3)	0.5 (2)	0.6 (3)		
	σ	0.064 (2)^a	0.067 (3)^b	^{b}	^{a}	^{a}	^{b}	^{b}	^{b}	1.3 (5)	16
	R (Å)	2.255	2.597	3.673	4.31	4.51	5.03	5.20	5.66		
1995)	*N*	4	4	4	8	4	4	4	8		

Table 5. Results of the shell-by-shell fitting procedure performed on the Fe *K*-edge data displayed in Fig. 4. The S_0^2 value used for the Feff calculation of phase-shift and amplitude functions is 1. *R* is the interatomic distance between the absorbing atom and the neighbouring shell, N is the number of atomic neighbours in the shell, and ΔE0 is the energy shift between the Feff8.1 threshold energy and the user-defined threshold energy. All parameter values followed by (a) and (b) are linked to the first parameter value placed above in the table. When using 8 phase-shift and amplitude functions, this approach gives 34 independent parameters and 19 free fitting parameters. The goodness of fit was estimated by a reduced chi-square indicator χ^2_R.

Comparison of the Fe *K*-edge XANES spectra of the Fe-S_0.5h and Fe-S_1510h (*i.e.* final nanocrystalline FeS_2) samples with that of the nanocrystalline biogenic Fe^{II}-mackinawite from Ikogou *et al*. (2017) gives information about the oxidation states and coordination of Fe in our samples (Fig. SI-5). According to the analysis of the Fe *K*-edge XANES spectra of Fe sulfides provided by Matamoros-Veloza *et al*. (2018a), the position of the first maximum in the edge is related to the contributions of Fe(II) and Fe(III). This maximum is found at 7122 eV in our Fe-S_0.5h sample and at 7121 eV in FeS-mackinawite or FeS_2-pyrite. This 1 eV shift to higher energy might indicate the occurrence of a minor but significant Fe(III) contribution in the Fe-S_0.5h sample compared to crystalline Fe^{II}-sulfides (Fig. SI-5). Additionally, in agreement with the observations reported by Matamoros-Veloza *et al*. (2018a), a noticeable energy shift of the pre-edge centroid and peak intensity is observed between the Fe-S_0.5h sample and nanocrystalline mackinawite. These trends could be interpreted in our sample as both a contribution of Fe(III) and changes/distortions of the Fe site (Wilke *et al.*, 2001). Finally, a post-edge shoulder contribution is observed between 7130-7140 eV on the Fe *K*-edge XANES spectrum of our Fe-S_0.5h sample (Fig. SI-5). This feature is not observed on the Fe *K*-edge XANES spectra of our Fe-S_1510h sample and the nanocrystalline biogenic Fe^{II}-mackinawite from Ikogou et al. (2017), in agreement with the data reported by Matamoros-Veloza *et al*. (2018a) for their “FeS_{Nano}” sample and in data at the Fe *K*-edge published for greigite by Watson *et al*., (2000).

Thus, XRD-Rietveld, WAXS-PDF and EXAFS analyses yield consistent and complementary information on the structure of the FeS precursors for pyrite in our batch synthesis experiments, giving evidence for at least two types of phases in approximately equal proportion (*i.e.* $FeS_{(nanoMck)}$ and $FeS_{(cluster)}$) and probably containing significant amount of Fe(III). This model, here represented with two components in a binary system might be better envisaged as a continuum in size between Fe_xS_x-clusters and poorly ordered nano-mackinawite, as proposed by Theberge and Luther (1997) and Rickard and Morse (2005).

DISCUSSION

Mineralogical precursors of pyrite

Fe *K*-edge EXAFS results shows that the local structure of the solid phase that forms during the first 30 minutes after reacting the acidic metal solutions with the Na_2S solution is similar for all samples collected prior to pyrite formation, regardless of the presence of Ni or As (Fig. 1, Table SI-2). Hence, the Ni:Fe or As:Fe ratio of 0.001 mol:mol we used did not significantly influence the mineralogical characteristics of the initial precursors of pyrite in our syntheses experiments. XRD-Rietveld and PDF-WAXS analyses performed on the Fe-S_0.5h sample indicate that this initial material actually corresponds to a mixture of compounds, that we modelled by two end-members (*i.e.* $FeS_{(nanoMck)}$ and $FeS_{(cluster)}$). The $FeS_{(nanoMck)}$ end-member is a nanocrystalline mackinawite that can be measured by

XRD, while the $FeS_{(cluster)}$ appears to be a colloidal form of FeS organised in domains smaller than 8 Å, as revealed by PDF-WAXS analysis.

Our observations on the structure of the $FeS_{(cluster)}$ phase forming in our batch experiments (Table 4), together with previous descriptions by Rickard and Luther (2007) and Noël *et al.* (2020) point towards colloidal FeS clusters of Fe_xS_x type. One hypothesis is that such Fe_xS_x clusters could have a single sheet-like structure, as described by Csákberényi-Malasics *et al.* (2012). In our case, the occurrence of FeS clusters with such a single sheet-like structure would be supported by the lack of observable inter-sheet Fe-Fe contribution in the *ab* plane at 3.67 Å (uncorrected for phase shift) in the FFT of the Fe *K*-edge EXAFS data (Table 5). A large variability in the domain dimensions of these precursors can be noted from the XRD and PDF analysis of these early-stage solids. As these clusters are small ($\leq$ 8 Å) and might be interwoven, folded and curved, it is difficult to determine a single ideal crystal structure. Michel *et al.* (2005) suggested that different degrees of aggregation of uniform nanocrystalline FeS particles are responsible for this distribution of crystallite sizes and structure. Matamoros-Veloza *et al.* (2018b) also pointed aggregation processes and reported that the morphology of these FeS species might depend on pH and reaction rate. These findings could converge with those of Wolthers *et al.* (2003) who described disordered FeS precipitates as a mixture of two FeS phases: MkA and MkB. MkA was described as sheet-like precipitated aqueous FeS clusters that could be compared with our $FeS_{(cluster)}$ phase, whereas MkB was likely more ordered such as our $FeS_{(NanoMck)}$.

Recently, an early-forming solid in Fe-S systems has been identified as a new phase and designated as FeS_{Nano} by Matamoros-Veloza *et al.* (2018a). This FeS_{Nano} phase that was stabilized in conditions close to those of our study (*i.e.* under anaerobic conditions and at pH <4.5) is composed of monosulfides (62%), polysulfides (17%), and disulfides (14%), as indicated by Raman spectroscopy. XPS measurements indicated the occurrence of both Fe(II) and Fe(III) in this compound and the authors proposed that initial Fe(II) atoms was oxidized with time to Fe(III) and that the release of Fe(II) to solution was equilibrated with the oxidation of H_2S by Fe(III) atoms. This suite of reactions was considered to result in the production of polysulfides at the solid/solution interface that would have further intercalated within the layered Fe-S structure. Polysulfides together with S(0) species are indeed well-known as the first oxidation products of FeS in oxic conditions (Boursiquot *et al.*, 2001). In addition, these species have also been evidenced by XPS as a thin weathering film at the surface of particles of crystalline mackinawite by Mullet *et al.* (2002). In the case of the new FeS_{Nano} species observed in anoxic conditions by Matamoros-Veloza *et al.* (2018a), we infer that the acidic media would have stabilized the polysulfides together with the Fe(II)/Fe(III) ratio in the solid. Thus, given our Fe *K*-edge XANES results on our FeS precursors, the occurrence of mixed Fe(II)/Fe(III) species within the proposed FeS continuum is suspected (Fig. SI-5). Moreover, the observed centroid shift in the pre-edge Fe *K*-edge XANES data with respect to pure Fe^{II}-mackinawite suggests the possible occurrence of octahedral Fe, more likely in the $FeS_{cluster}$ fraction of the FeS precursors. This latter hypothesis has to be considered with respect to the known occurrence of octahedral Fe(II)/Fe(III) and Fe(II) in greigite and pyrite, respectively (Matamoros-Veloza et al., 2018a).

Mechanism of pyrite formation

At room temperature, the reactions that lead to pyrite formation generally involve a Fe monosulfide (FeS) precursor (Berner, 1970; Rickard, 1975). In our synthesis route, similar to that of Wei and Osseo-Asare (1997), Noël (2014), Morin *et al.*, (2017) and Le Pape *et al.* (2017), Fe(III) species rapidly react with $H_2S_{(aq)}$ to form $FeS_{(solid)}$, $S(0)_{(\alpha\text{-sulfur})}$ and remaining $Fe^{2+}_{(aq)}$. The synthesis procedure starts from an acidic ferric solution that is mixed with an alkaline Na_2S solution, which prompts us to write the first step of the synthesis as follows, even if the working pH range of our experiments is pH 3.7 – 5.8 after the mixing of the reactants (*i.e.* above the first hydrolysis constant of $Fe(III)_{(aq)}$ p$K\!a$ = 2.0):

$$Fe^{3+}_{(aq)} + HS^{-}_{(aq)} \rightarrow \tfrac{1}{2}\,Fe^{2+}_{(aq)} + \tfrac{1}{2}\,FeS_{(cluster,\ nanoMck)} + \tfrac{1}{2}\,S(0)_{(\alpha\text{-sulfur})} + H^{+}_{(aq)} \qquad (1)$$

The net proton release in reaction 1 explains the decrease in pH that is observed in the course of our batch experiments (Table 1, Table SI-1, Fig. SI-1). However, our results show that the $FeS_{(cluster)}$ and $FeS_{(nanoMck)}$ phases, or a continuum between these two end-members, as well as $S(0)_{(\alpha\text{-sulfur})}$, are formed within the first 30 min of reaction (Fig. 1, 3 and 4, Tables 2, 3 and 4). This latter result questions the origin of the continuous pH decrease that is observed during our pyrite synthesis experiments (Fig. SI-1).

The $FeS_{(cluster,\ nanoMck)}$ phases then react with $S(0)_{(\alpha\text{-sulfur})}$ to produce pyrite, likely via a polysulfide $H_2S_{n(aq)}$ and $Fe_xS_{x(aq)}$ pathway (Rickard, 1975; Luther, 1991; Theberge and Luther, 1997; Rickard and Morse, 2005; Rickard and Luther, 2007). More precisely, Fe_xS_x clusters, that can be in equilibrium with $FeS_{(cluster,\ nanoMck)}$ phases (*i.e.* the $FeS_{(solid)}$ precursors) in concentrated media, are oxidized by $H_2S_{n(aq)}$ aqueous polysulfides (*i.e.* likely in equilibrium with $S(0)_{(\alpha\text{-sulfur})}$) and thus convert into FeS_2:

$$Fe_xS_{x(aq)} + H_2S_{n(aq)} \rightarrow Fe_{x-1}S_{x-1(aq)} + H_2S_{n-1} + FeS_{2(pyrite)} \qquad (2)$$

$Fe_xS_{x(aq)}$ clusters may directly derive from the $FeS_{(cluster,\ nanoMck)}$ phases within a continuous size distribution, as proposed by Rickard and Morse (2005), in agreement with the molecular-scale (≤ 8 Å) and colloidal-scale (≤ 4 nm) sizes that we determined for the $FeS_{(cluster)}$ and $FeS_{(nanoMck)}$ phases, respectively. The fact that we collected the $FeS_{(cluster)}$ phase by regular centrifugation (6000 rpm) from our synthesis experiment media is likely made possible by the aggregation of these clusters in our high ionic strength suspensions (Cornwell and Morse, 1987).

As already mentioned, although not directly observed in our experiments, polysulfides cannot be excluded from S *K*-edge XANES analysis of the solid phase. These molecules are actually known as aqueous species (Rickard and Morse 2005 ; Rickard and Luther 2007) but they can also be associated with FeS surfaces (Boursiquot *et al.*, 2001; Mullet *et al.*, 2002; Matamoros-Veloza *et al.*, 2018a). Although not analyzed in our batch suspensions and not firmly observed in the solid phase, aqueous polysulfide species ($H_2S_{n(aq)}$) could potentially form via reduction of Fe(III) by HS^- at the start of the synthesis, as also proposed by Morin *et al.* (2017). Assuming the same conditions as for reaction 1, one may propose here the following reaction:

$$Fe^{3+}_{(aq)} + n/[2(n-1)]\ HS^-_{(aq)} \rightarrow Fe^{2+}_{(aq)} + 1/[2(n-1)]\ H_2S_{n(aq)} + (n-2)/[2(n-1)]\ H^+_{(aq)} \qquad (3)$$

Accordingly, Avetisyan *et al*. (2019) proposed that in marine sediment at pH > 7, direct formation of polysulfides upon oxidation of hydrogen sulfide by Fe(III)-bearing minerals (similar to Reaction 3) is more likely than polysulfide production via reductive dissolution of $S(0)_{(\alpha\text{-sulfur})}$ by $H_2S_{(aq)}$ (Reaction 4). Indeed, this latter reaction is as slow as 1.3 years under diagenetic conditions, and is not thermodynamically favoured in our acidic pH conditions (pH 3.7-5.8) (Boulègue and Michard, 1978; Rickard and Morse, 2005; Rickard and Luther, 2007):

$$(n\text{-}1)\ S(0)_{(\alpha\text{-sulfur})} + H_2S_{(aq)} \Leftrightarrow H_2S_{n(aq)} \qquad (4)$$

However, in our experiments, about half of the HS^-, introduced in equimolar concentrations with $Fe^{3+}_{(aq)}$ in the medium is rapidly oxidized to S(0) (Reaction 1), as observed by XRD (Fig. 4a) and S *K*-edge XANES analysis (Fig. 3). Meanwhile, almost all $Fe^{3+}_{(aq)}$ is reduced to $Fe^{2+}_{(aq)}$, which limits the formation of polysulfides through reaction 3, and *a fortiori* reaction 4. Nevertheless, a fraction of Fe^{3+} is likely incorporated within the instantaneously precipitated FeS solids (Fig. SI-5). Thus, it cannot be excluded that a fraction of the initial S(-II) and Fe(III) pool remains unreacted, and thus that a minor amount of polysulfides could be further produced via the reduction of the solid-bound Fe(III) by aqueous H_2S (similar to reaction 3), even after FeS precipitation. Such reaction could thus contribute to the pH decrease observed during the synthesis (Fig. SI-1). This route would be in agreement with the mechanism proposed by Matamoros-Veloza *et al.* (2018a) for the formation of FeS_{Nano}.

Eventually, the formation of polysulfide species from reaction 4, is necessarily limited by the availability of S(-II), assumed to be quantitatively consumed by reactions 1 and 3. However, once initiated, the production of oxidized polysulfide species (high *n*) can be maintained by the reaction of $S(0)_{(\alpha\text{-sulfur})}$ with reduced polysulfide species (low *n*) produced by pyrite formation (Eq. 2), as follows (Rickard and Morse, 2005):

$$S(0)_{(\alpha\text{-sulfur})} + H_2S_{n-1(aq)} \Leftrightarrow H_2S_{n(aq)} \qquad (5)$$

Moreover, the availability of $S(0)(\alpha\text{-sulfur})$ may promote the formation of higher-*n* polysulfide species:

$$S(0)(\alpha\text{-sulfur}) + H_2S_{n(aq)} \Leftrightarrow H_2S_{n+1(aq)} \quad (5bis)$$

Hence, since the first p*Ka* of polysulfide species decreases with *n* (Schoonen and Barnes, 1988; Kamyshny *et al.*, 2004; Rickard and Morse, 2005), one may infer that, for $n \geq 2$ and $pH > 5$, $n \geq 3$ and $pH > 4.2$, $n \geq 4$ and $pH > 3.8$ or $n \geq 5$ and $pH \geq 3.5$, the higher-*n* polysulfide species may deprotonate in the pH range (pH 3.7 – 5.8) of our synthesis experiments :

$$H_2S_{n(aq)} \Leftrightarrow HS_{n\ (aq)}^{-} + H^{+}_{(aq)} \quad (6)$$

Reactions (5, 5bis and 6) could then also explain the continuous decrease in pH we observe over the course of pyrite formation (Fig. SI-1). Hence, since polysulfides are suspected to be key drivers of the pH decrease in our batch synthesis experiments, one may suggest that pyrite nucleation from the FeS particles continuum could be activated by polysulfide species in solution and/or in contact with the FeS surfaces.

Influence of Ni and As on pyrite nucleation and growth

This study pursues Wolthers *et al.* (2007), Morin *et al.* (2017) and Le Pape *et al.*(2017) studies, which highlighted the accelerating influence of Ni and inhibiting influence of As on pyrite formation. However, in these former studies, the Ni and As aqueous concentrations were higher than in the batch synthesis experiments conducted in the present study. To this regard, our results clearly confirm and define in time the antagonistic effects of Ni and As on pyrite formation kinetics, when these impurities occur at trace level (*i.e.* in the thousands of ppm range). The mineral sequence observed in our batch synthesis experiments indicates that the actual nature of the mineral phases formed before pyrite is the same without or with Ni or As. Indeed, a $FeS_{(cluster,\ nanoMck)}$ continuum and S(0) formed at the beginning of the batch synthesis experiments and their interactions lead to pyrite formation, likely in the presence of polysulfide species as suggested by the continuous pH decrease discussed in the previous section. Such unicity of the pyrite precursors phases implies that the incorporation of Ni and As into pyrite depends on the interaction of these impurities with the $FeS_{(cluster,\ nanoMck)}$ precursors, the pyrite nuclei and/or the associated polysulfides. Indeed, some publications have suggested that trace elements can also interact locally with polysulfides (Morse *et al.*, 1987; Akiyama *et al.*, 2017).

Morse and Arakaki (1993) and Wilkin and Beak (2017) have shown that Ni is able to sorb at the mackinawite surface. However, in both studies, Ni was added in solution to the mackinawite previously formed, which differs from our experimental setup. Based on first principles calculations, Kwon *et al.* (2015) reported that Ni^{2+} for Fe^{2+} substitution in the mackinawite structure is energetically favourable, which is also consistent with their same valence and close ionic radius (Shannon, 1976). This substitution was recently evidenced in both abiotic (Wilkin and Beak 2017) and biogenic (Ikogou *et al.*, 2017) mackinawite. Wilkin and Beak (2017) also reported that the reaction between Ni-mackinawite and polysulfides led to pyrite formation with Ni retention in the solid phase, this process being detailed by Morin *et al*. (2017). These latter authors showed that Ni^{2+} ions in the initial solution accelerates pyrite formation by favouring the nucleation of Ni-rich pyrite nuclei that form the cores of the pyrite nanocrystals produced at room temperature. Conversely, Swanner *et al*. (2019) observed a partial inhibition of pyrite formation when Ni was initially present in FeS_m solids compared to similar experiments without Ni. These authors concluded that both Ni and Co substitution in FeS_m could slow down pyrite formation. This observed opposite behaviour could depend on the speciation of Ni associated to the FeS precursors and on their degree of crystallinity before transformation into pyrite. Indeed, under our experimental conditions at low temperature and with Fe^{3+} in the starting solution, Ni could be present both as amorphous NiS and Ni^{2+} substituting for Fe^{2+} in FeS, as shown by EXAFS analysis at the Ni K-edge by Morin *et al.* (2017) for similar conditions but with 10 times more Ni. It is also likely that NiS and (Fe,Ni)S particles would have remained nanosized all along the synthesis experiments. Indeed, although ripening of $(Fe,Ni)S_{(mackinawite)}$ is accelerated by the presence of Ni, which could inhibit further transformation into pyrite, this process takes several weeks at ambient temperature (Ikogou *et al.* 2017). Hence, nucleation of Ni-rich pyrite from NiS may accelerate pyrite formation in our experiments (Morin *et al.* 2017), and ripening of $(Fe,Ni)S_{(mackinawite)}$ (Ikogou *et al.* 2017), albeit slow at ambient temperature, could explain the persistence of some FeS in the Fe-S:Ni synthesis end products (Fig. 1 and 3 ; Tables 2 and 3). Under the experimental conditions at 65°C reported by Swanner *et al.*, (2019), mackinawite could have partly crystallized making it more recalcitrant than unsubstituted mackinawite to further transformation into pyrite.

Nonetheless, the present study confirms the accelerated formation of pyrite in Ni-doped solutions and unambiguously shows that this kinetic effect is still effective at trace levels. This latter point strongly suggests that Ni incorporation into the FeS precursors (Morin *et al*., 2017) facilitates pyrite formation. Matamoros-Veloza *et al.* (2018b) have suggested that the expanded layered structure of the FeS_{Nano} phase they identified could facilitate the incorporation of trace metals in between the layers. Although the possible sorption or layer intercalation of Ni within nano-mackinawite (Kwon *et al.*, 2015) cannot be excluded, results from previous XAS studies at the Ni *K*-edge show that the major part of Ni is clearly substituting for Fe in the FeS precursors (Wilkin and Beak, 2017; Morin *et al*., 2017). In particular, one may infer that Ni for Fe substitution in the colloidal $FeS_{(cluster)}$ phase (*i.e.* aggregated Fe_xS_x clusters) may accelerate reaction (2), which also involves polysulfide species. The mechanisms of this acceleration is still unclear and it may either rely on ligand-exchange rates (Morse and Luther, 1999) and/or on enhanced electron transfers (Noël *et al*. 2020) due to the metallic character of FeS (Devey *et al.*, 2008). Indeed, local Ni incorporation in the Fe-rich *ab* plane could possibly increase the delocalization of *d* electrons from the valence to the conduction band (Vaughan and Ridout, 1971).

Several studies have shown that As can substitute for both S and Fe atoms in the pyrite structure (Savage *et al*., 2000; Scholz and Neumann, 2007; Deditius *et al*., 2008; Gregory *et al*., 2015; Le Pape *et al*., 2017; Manceau *et al*., 2020). However, the mechanisms at the molecular level of this incorporation during pyrite formation at ambient temperature is still unclear. Some studies that have addressed solid-solution interactions of As with FeS suggested that As sorbs onto this phase rather than being incorporated in its structure (Kirk *et al*., 2010; Saunders *et al*., 2018). Saunders *et al*. (2018) proposed that sorption of As(III) involves inner-sphere complexation, inducing long-term arsenic retention. Farquhar *et al*. (2002) suggested outer-sphere complexation of As on both mackinawite and pyrite surfaces and reported As_2S_3 precipitation in some of their experiments. In experiments performed in presence of As(III) and mackinawite, Niazi and Burton (2016) pointed out the formation of As_2S_3-like species and the possible occurrence of As(V) under strict anoxia, which can be further interpreted as the result of a possible occurrence of thioarsenate species. Bostick and Fendorf (2003) reported the reduction of As(V) to As(III) on Fe-S surfaces and measured a Fe-As-S molecular association similar to that observed in arsenopyrite. Finally, in a recent study on the formation of synthetic As-bearing pyrite at temperature > 80°C, Ma *et al*. (2020) proposed a three steps reaction with As sorption onto FeS, then As release upon FeS dissolution, and finally As incorporation into pyrite mainly as As(II/III). Thus, no clear mechanism can be easily extracted from the literature concerning As behaviour towards Fe-S surfaces in sulfidic conditions. This lack of consensus is probably related to the complex geochemical behaviour of As in such conditions because of the numerous possible, and still debated (Wilkin *et al*., 2019; Planer-Friedrich, 2020), chemical forms of this element (Couture and Van Cappellen, 2011).

After showing that As can inhibit the formation of pyrite from mackinawite, Wolthers *et al*. (2007) proposed that As sorption sites must be crucial for further Fe(II) sulfide transformation mechanisms. The deceleration of pyrite formation that we observed in our study is in agreement with this hypothesis, even with trace amounts of As. Therefore, we could infer that As(III) species bound to $FeS_{(nanoMck)}$ and $FeS_{(cluster)}$ could hinder their reaction with polysulfide species. Also, As(III) could bind to pyrite nuclei and inhibit their growth, by shielding surface sites. Another possibility is that the local formation of amorphous As_2S_3 would passivate the mineral surfaces and thus slow down both the conversion of FeS into pyrite and/or pyrite crystal growth. An alternative explanation would be that As(III) could partly remain in solution after being sulfidized or oxidized by polysulfides or S(0), resulting in the formation of oxythio-As species (Couture and Van Cappellen, 2011). Such oxythio-As species could then sorb to the FeS surfaces, or possibly interact directly in solution with polysulfide species, thus inhibiting the nucleation mechanism. Finally, one can infer that under our conditions of synthesis that are sufficient to reduce aqueous As(III) to As(-I) when incorporated in pyrite (Le Pape *et al*., 2017), As could also be incorporated into polysulfide chains for instance as AsS_n^- ($5 \leq n \leq 8$; Zhang *et al*., 2014), starting for instance by the formation of the As-S dianion pair, as it is finally observed in pyrite (Blanchard *et al.*, 2007). Such a process would possibly change the polysulfides access to the FeS surfaces and thus delay pyrite formation.

Environmental and geological implications

Since the present experiments were carried out at ambient temperature, our results may have implications on our understanding of the role of Fe sulfide transformations in the cycling of Ni and As in euxinic environments. The uptake of Ni or As by Fe sulfides has been described previously by Morse and Arakaki (1993) and Gallegos *et al.* (2007) respectively. Their works have pointed out the ability of FeS to withdraw these elements from natural environments under anoxic conditions *via* sorption and coprecipitation processes. Indeed, Ni and As sorption and As co-precipitation with FeS are known as efficient ways for removing these contaminants from solution (Farquhar *et al*., 2002; Gallegos *et al*., 2007; Gong *et al*., 2016; Liang *et al*., 2019). However, recent works by Noel *et al.* (2020) have demonstrated that FeS clusters could remain suspended during long periods of time in groundwater systems, enhancing the fluxes of Fe and S in these environments and thus affecting the dynamic of associated trace elements. In addition, the present study shows that the occurrence of trace amounts of Ni or As has a significant influence on the kinetics of the transformation of FeS clusters and nano-mackinawite into pyrite. This could mean that the persistence of mobile colloidal FeS species might depend on the actual nature of the trace elements occurring in the system. For instance, one may expect that the binding of As to colloidal FeS clusters or the co-occurrence of thio-As complexes would favour their persistence and thus facilitate As transport. Indeed, it has been shown that colloids can be the main vehicle for the transport of several pollutants in aqueous systems and soils (Pédrot *et al*. 2008). Wolthers *et al.* (2005) has successfully predicted the transport and immobilization of As in anoxic environments based on the measurements of sorption isotherms. Coupled with their findings, our results suggest that As sorption onto FeS clusters can slow down the sequestration of this pollutant into more stable pyrite and thus maintain its mobility. In contrast, the presence of Ni would accelerate the conversion of FeS clusters into pyrite and thus decrease the mobility of this pollutant. Nevertheless, changes in pH and redox potential could accelerate desorption, partitioning and oxidation of associated pollutants, depending on the sediment and environmental conditions (Eggleton and Thomas, 2004). Pollutants associated with pyrite at trace levels can be potentially released when pyrite is oxidized by resuspension of sediments or during seasonal changes in redox states. For instance Hatje *et al*. (2003) have shown that desorption occurred more often in seawater than in freshwater for some sorbed elements (Cd, Zn and Co), making it clear that pH, salinity and concentrations have major influence on the cycling of pollutants. As discussed by Holmes (1999), we cannot exclude different oxidation pathways in naturally occurring mackinawite. Especially, the larger surface to volume ratio of mackinawite coatings could allow a faster oxidation than in synthesis experiments. In a study on the susceptibility of Ni(II)-bearing pyrite to oxidation, Liang *et al*. (2019) reported an increasing oxidation kinetics with increasing Ni(II) incorporation. This trend was considered to be related to specific sulfur defects. Conversely, these authors showed that Ni(II) sorption onto pyrite surface could yield a shielding effect on defect sites and decrease the oxidation susceptibility of pyrite.

Impact on paleo-reconstructions of ancient environments

In addition to these environmental implications, trace element patterns in sedimentary pyrite are often used to constrain the redox and compositional parameters of ancient environments (Huerta-Diaz and Morse, 1992; Tribovillard *et al.*, 2006; Large *et al.*, 2014; Gregory *et al.*, 2015; Large *et al.*, 2017). Here, we confirm that the presence of trace element impurities in the pyrite precipitation medium influences pyrite formation kinetics, which could have an influence on some environmental and/or geological paleo-reconstructions. As Algeo and Li (2020) and Algeo and Liu (2020) explained, proxies cannot be considered as universally reliable and should be used on a sediment- and formation-specific basis, with a re-calibration given for each studied system. We suggest that the chemical composition of the studied mineral also has to be taken into account, as it might accelerate or delay its formation rate in aqueous solutions. We can consider that kinetics of pyrite formation and its sequestration capacity towards trace elements could have an impact on their apparent partition coefficient between solid and solution in ancient sedimentary records. For instance, as suggested by Morin et al. (2017), rapid precipitation of Ni-rich pyrite in marine sediments could be responsible for the drastically lowered Ni/Fe ratio of the Archean ocean (Konhauser et al., 2009). Another important point that has to be considered is the nature of the precursor phases of the studied mineral, which could be responsible for an enhanced mobilization of trace elements prior to its formation.

CONCLUSIONS

It is widely accepted that pyrite mainly forms by Fe monosulfide (FeS) oxidation. In this experimental study, we demonstrated that the pyrite precursors obtained from coprecipitation of Fe(III) with HS^- are not crystalline mackinawite but rather consist in a continuum between nanocrystalline mackinawite and FeS clusters, likely similar to the Fe_2S_2 to $Fe_{150}S_{150}$ continuum proposed by Rickard and Morse (2005).

In this study, Ni and As were introduced in the aqueous medium at trace concentration, which is roughly comparable to natural conditions that prevail in pore-scale micro-environments in diagenetic sulfidic (sub-)surface sediments. Yet, the impact of these trace elements on pyrite formation kinetics is significant in the thousand ppm range with a major acceleration of pyrite formation in the Ni-doped system and an inhibition in the As-doped one. Furthermore, under the light of previous studies by Morin *et al*. (2017), Le Pape *et al*. (2017) and Wilkin and Beak (2017), the results of the present study confirm that Ni and As interact with both the pyrite precursors and pyrite nuclei, possibly involving polysulfides and thus having a strong influence on pyrite nucleation.

Further investigations will be necessary to determine whether the mineralogical precursors identified in the present study are also found in sulfidic environments in diagenetic sediments. Such an uptake of Ni and As by pyrite precursors during diagenesis, as well as Ni-aceleration and As-deceleration on pyrite formation are expected to have a significant impact on the use of pyrite signal in (paleo-)environmental studies. From an environmental perspective, these mechanisms are indeed expected to decrease the concentration of these potentially toxic elements in aqueous solutions, which may have a major impact on the quality of anoxic waters. From a geological perspective, they might potentially drive the pyrite signature that is used for paleo-reconstructions. If confirmed, this latter influence should be further taken into consideration when pyrite composition is translated in terms of ancient environments and past climates.

ACKNOWLEDGEMENTS.

We thank the SOLEIL and SSRL Synchrotrons for having provided beamtime. We are grateful to E. Fonda, G. Alizon, and A. Zitolo for their help in the EXAFS experiments at the SAMBA beamline and S. Blanchandin for her help in glove-box operation. The staff of the CRISTAL beamline is acknowledged for help during WAXS-PDF measurements. The authors are indebted to P. Rosier, for having designed dedicated cryogenic temperature EXAFS sample holders, L. Delbès for his help in XRD measurements. We also thank M. Latimer and E. Nelson for their assistance during XANES measurements at SSRL beamline 4-3. We also thank G. Tang for her assistance in laboratory experiments at SSRL. Use of the Stanford Synchrotron Radiation Lightsource, SLAC National Accelerator Laboratory, is supported by the U.S. Department of Energy, Office of Science, Office of Basic Energy Sciences under Contract No. DE-AC02-76SF00515. This work was supported by the Programme National de Planétologie (PNP) of CNRS/INSU, co-funded by CNES. This work has been conducted in the framework of the PhD thesis of C. Baya at ED 398 GRNE, Sorbonne University.

REFERENCES

Akiyama M., Shinkai Y., Unoki T., Shim I., Ishii I. and Kumagai Y. (2017) The Capture of Cadmium by Reactive Polysulfides Attenuates Cadmium-Induced Adaptive Responses and Hepatotoxicity. *Chem. Res. Toxicol.* **30**, 2209–2217.

Algeo T. J. and Li C. (2020) Redox classification and calibration of redox thresholds in sedimentary systems. *Geochimica et Cosmochimica Acta*. Available at: http://www.sciencedirect.com/science/article/pii/S0016703720300788 [Accessed June 7, 2020].

Algeo T. J. and Liu J. (2020) A re-assessment of elemental proxies for paleoredox analysis. *Chemical Geology* **540**, 119549.

Ankudinov A. L., Ravel B., Rehr J. J. and Conradson S. D. (1998) Real-space multiple-scattering calculation and interpretation of x-ray-absorption near-edge structure. *Phys. Rev. B* **58**, 7565–7576.

Avetisyan K., Buchshtav T. and Kamyshny A. (2019) Kinetics and mechanism of polysulfides formation by a reaction between hydrogen sulfide and orthorhombic cyclooctasulfur. *Geochimica et Cosmochimica Acta* **247**, 96–105.

Benning L. G., Wilkin R. T. and Barnes H. L. (2000) Reaction pathways in the Fe–S system below 100°C. *Chemical Geology* **167**, 25–51.

Berar J.-F. and Baldinozzi G. (1998) XND code: From X-ray laboratory data to incommensurately modulated phases. Rietveld modeling of complex materials. *CPD Newsletter* **20**, 3–5.

Berner R. A. (1970) Sedimentary pyrite formation. *Am J Sci* **268**, 1–23.

Blanchard M., Alfredsson M., Brodholt J., Wright K. and Catlow C. R. A. (2007) Arsenic incorporation into FeS2 pyrite and its influence on dissolution: A DFT study. *Geochimica et Cosmochimica Acta* **71**, 624–630.

Bostick B. C. and Fendorf S. (2003) Arsenite sorption on troilite (FeS) and pyrite (FeS2). *Geochimica et Cosmochimica Acta* **67**, 909–921.

Boulègue J. and Michard G. (1978) Constantes de formation des ions polysulfures S-26, S-25 et S-24 en phase aqueuse. *Journal français d’hydrologie* **9**, 27–33.

Bourdoiseau J.-A., Jeannin M., Rémazeilles C., Sabot R. and Refait P. (2011) The transformation of mackinawite into greigite studied by Raman spectroscopy. *Journal of Raman Spectroscopy* **42**, 496–504.

Boursiquot S., Mullet M., Abdelmoula M., Génin J.-M. and Ehrhardt J.-J. (2001) The dry oxidation of tetragonal FeS1-xmackinawite. *Phys Chem Min* **28**, 600–611.

Briois V., Fonda E., Belin S., Barthe L., Fontaine C. L., Langlois F., Ribbens M. and Villain F. (2011) SAMBA: The 4–40 keV X-ray absorption spectroscopy beamline at SOLEIL. In *UVX 2010 - 10e Colloque sur les Sources Cohérentes et Incohérentes UV, VUV et X ; Applications et Développements Récents* UVX 2010 - 10e Colloque sur les Sources Cohérentes et Incohérentes UV, VUV et X ; Applications et Développements Récents. EDP Sciences. pp. 41–47. Available at: https://uvx.edpsciences.org/articles/uvx/abs/2011/01/uvx2011_006/uvx2011_006.html [Accessed July 1, 2020].

Cornwell J. C. and Morse J. W. (1987) The characterization of iron sulfide minerals in anoxic marine sediments. *Marine Chemistry* **22**, 193–206.

Couture R.-M. and Van Cappellen P. (2011) Reassessing the role of sulfur geochemistry on arsenic speciation in reducing environments. *Journal of Hazardous Materials* **189**, 647–652.

Csákberényi-Malasics D., Rodriguez-Blanco J. D., Kis V. K., Rečnik A., Benning L. G. and Pósfai M. (2012) Structural properties and transformations of precipitated FeS. *Chemical Geology* **294–295**, 249–258.

Deditius A. P., Utsunomiya S., Renock D., Ewing R. C., Ramana C. V., Becker U. and Kesler S. E. (2008) A proposed new type of arsenian pyrite: Composition, nanostructure and geological significance. *Geochimica et Cosmochimica Acta* **72**, 2919–2933.

Devey A. J., Grau-Crespo R. and de Leeuw N. H. (2008) Combined Density Functional Theory and Interatomic Potential Study of the Bulk and Surface Structures and Properties of the Iron Sulfide Mackinawite (FeS). *J. Phys. Chem. C* **112**, 10960–10967.

Egami T. and Billinge S. J. L. (2003) *Underneath the Bragg Peaks: Structural Analysis of Complex Materials*., Elsevier.

Eggleton J. and Thomas K. V. (2004) A review of factors affecting the release and bioavailability of contaminants during sediment disturbance events. *Environment International* **30**, 973–980.

Farquhar M. L., Charnock J. M., Livens F. R. and Vaughan D. J. (2002) Mechanisms of Arsenic Uptake from Aqueous Solution by Interaction with Goethite, Lepidocrocite, Mackinawite, and Pyrite: An X-ray Absorption Spectroscopy Study. *Environ. Sci. Technol.* **36**, 1757–1762.

Farrow C. L., Juhas P., Liu J. W., Bryndin D., Božin E. S., Bloch J., Proffen T. and Billinge S. J. L. (2007) PDFfit2 and PDFgui: computer programs for studying nanostructure in crystals. *J. Phys.: Condens. Matter* **19**, 335219.

Farrow C. L. and Billinge S. J. L. (2009) Relationship between the atomic pair distribution function and small-angle scattering: implications for modeling of nanoparticles. *Acta Cryst A* **65**, 232–239.

Figueroa M. C., Gregory D. D., Lyons T. W. and Williford K. H. (2017) Isotopic and elemental chemistry of sedimentary pyrite: A combined analytical and statistical approach to a novel planetary biosignature. *AGU Fall Meeting Abstracts* **43**. Available at: http://adsabs.harvard.edu/abs/2017AGUFM.P43G..07F [Accessed July 1, 2020].

Gallegos T. J., Hyun S. P. and Hayes K. F. (2007) Spectroscopic Investigation of the Uptake of Arsenite from Solution by Synthetic Mackinawite. *Environ. Sci. Technol.* **41**, 7781–7786.

Gong Y., Tang J. and Zhao D. (2016) Application of iron sulfide particles for groundwater and soil remediation: A review. *Water Research* **89**, 309–320.

Gregory D. D., Large R. R., Halpin J. A., Baturina E. L., Lyons T. W., Wu S., Danyushevsky L., Sack P. J., Chappaz A., Maslennikov V. V. and Bull S. W. (2015) Trace Element Content of Sedimentary Pyrite in Black Shales. *Economic Geology* **110**, 1389–1410.

Gregory D. D., Lyons T. W., Large R. R., Jiang G., Stepanov A. S., Diamond C. W., Figueroa M. C. and Olin P. (2017) Whole rock and discrete pyrite geochemistry as complementary tracers of ancient ocean chemistry: An example from the Neoproterozoic Doushantuo Formation, China. *Geochimica et Cosmochimica Acta* **216**, 201–220.

Hatje V., Payne T. E., Hill D. M., McOrist G., Birch G. F. and Szymczak R. (2003) Kinetics of trace element uptake and release by particles in estuarine waters: effects of pH, salinity, and particle loading. *Environment International* **29**, 619–629.

Holmes J. (1999) Fate of incorporated metals during mackinawite oxidation in sea water. *Applied Geochemistry* **14**, 277–281.

Huerta-Diaz M. A. and Morse J. W. (1992) Pyritization of trace metals in anoxic marine sediments. *Geochimica et Cosmochimica Acta* **56**, 2681–2702.

Ikogou M., Ona-Nguema G., Juillot F., Le Pape P., Menguy N., Richeux N., Guigner J.-M., Noël V., Brest J., Baptiste B. and Morin G. (2017) Long-term sequestration of nickel in mackinawite formed by Desulfovibrio capillatus upon Fe(III)-citrate reduction in the presence of thiosulfate. *Applied Geochemistry* **80**, 143–154.

Jeong H. Y., Lee J. H. and Hayes K. F. (2008) Characterization of synthetic nanocrystalline mackinawite: Crystal structure, particle size, and specific surface area. *Geochimica et Cosmochimica Acta* **72**, 493–505.

Kamyshny A., Goifman A., Gun J., Rizkov D. and Lev O. (2004) Equilibrium Distribution of Polysulfide Ions in Aqueous Solutions at 25 °C: A New Approach for the Study of Polysulfides' Equilibria. *Environ. Sci. Technol.* **38**, 6633–6644.

Kirk M. F., Roden E. E., Crossey L. J., Brealey A. J. and Spilde M. N. (2010) Experimental analysis of arsenic precipitation during microbial sulfate and iron reduction in model aquifer sediment reactors. *Geochimica et Cosmochimica Acta* **74**, 2538–2555.

Konhauser K. O., Pecoits E., Lalonde S. V., Papineau D., Nisbet E. G., Barley M. E., Arndt N. T., Zahnle K. and Kamber B. S. (2009) Oceanic nickel depletion and a methanogen famine before the Great Oxidation Event. *Nature* **458**, 750–753.

Konhauser K. O., Lalonde S. V., Planavsky N. J., Pecoits E., Lyons T. W., Mojzsis S. J., Rouxel O. J., Barley M. E., Rosìere C., Fralick P. W., Kump L. R. and Bekker A. (2011) Aerobic bacterial pyrite oxidation and acid rock drainage during the Great Oxidation Event. *Nature* **478**, 369–373.

Krause M. O. and Oliver J. H. (1979) Natural widths of atomic K and L levels, Kα X- ray lines and several KLL Auger lines. *Journal of Physical and Chemical Reference Data* **8**, 329–338.

Kwon K. D., Refson K. and Sposito G. (2015) Transition metal incorporation into mackinawite (tetragonal FeS). *American Mineralogist* **100**, 1509–1517.

Large R., Thomas H., Craw D., Henne A. and Henderson S. (2012) Diagenetic pyrite as a source for metals in orogenic gold deposits, Otago Schist, New Zealand. *New Zealand Journal of Geology and Geophysics* **55**, 137–149.

Large R. R., Halpin J. A., Danyushevsky L. V., Maslennikov V. V., Bull S. W., Long J. A., Gregory D. D., Lounejeva E., Lyons T. W., Sack P. J., McGoldrick P. J. and Calver C. R. (2014) Trace element content of sedimentary pyrite as a new proxy for deep-time ocean–atmosphere evolution. *Earth and Planetary Science Letters* **389**, 209–220.

Large R. R., Mukherjee I., Gregory D. D., Steadman J. A., Maslennikov V. V. and Meffre S. (2017) Ocean and Atmosphere Geochemical Proxies Derived from Trace Elements in Marine Pyrite: Implications for Ore Genesis in Sedimentary Basins. *Economic Geology* **112**, 423–450.

Le Pape P., Blanchard M., Brest J., Boulliard J.-C., Ikogou M., Stetten L., Wang S., Landrot G. and Morin G. (2017) Arsenic Incorporation in Pyrite at Ambient Temperature at Both Tetrahedral S $^{-I}$ and Octahedral Fe ^{II} Sites: Evidence from EXAFS–DFT Analysis. *Environ. Sci. Technol.* **51**, 150–158.

Lennie A. R., Redfern S. A. T., Schofield P. F. and Vaughan D. J. (1995) Synthesis and Rietveld crystal structure refinement of mackinawite, tetragonal FeS. *Mineralogical Magazine* **59**, 677–683.

Liang Z.-S., Song B.-D., Liu Y.-L., Liu Y., Ren H.-T., Wu S.-H., Jia S.-Y. and Han X. (2019) Reactivity Comparison of Different Ni(II)-Pyrites during Oxidative Dissolution under Acidic and pH-Neutral Conditions. *ACS Earth Space Chem.* **3**, 1096–1108.

Luther G. W. (1991) Pyrite synthesis via polysulfide compounds. *Geochimica et Cosmochimica Acta* **55**, 2839–2849.

Ma C., Zhang G., Chen J., Wang Q. and Liu F. (2020) Transfer of FeS-bound arsenic into pyrite during the transformation of amorphous FeS to pyrite. *Applied Geochemistry*, 104645.

Maillot F., Morin G., Wang Y., Bonnin D., Ildefonse P., Chaneac C. and Calas G. (2011) New insight into the structure of nanocrystalline ferrihydrite: EXAFS evidence for tetrahedrally coordinated iron(III). *Geochimica et Cosmochimica Acta* **75**, 2708–2720.

Maillot F., Morin G., Juillot F., Bruneel O., Casiot C., Ona-Nguema G., Wang Y., Lebrun S., Aubry E., Vlaic G. and Brown G. E. (2013) Structure and reactivity of As(III)- and As(V)-rich schwertmannites and amorphous ferric arsenate sulfate from the Carnoulès acid mine drainage, France: Comparison with biotic and abiotic model compounds and implications for As remediation. *Geochimica et Cosmochimica Acta* **104**, 310–329.

Matamoros-Veloza A., Cespedes O., Johnson B. R. G., Stawski T. M., Terranova U., de Leeuw N. H. and Benning L. G. (2018a) A highly reactive precursor in the iron sulfide system. *Nat Commun* **9**, 3125.

Matamoros-Veloza A., Stawski T. M. and Benning L. G. (2018b) Nanoparticle Assembly Leads to Mackinawite Formation. *Crystal Growth & Design* **18**, 6757–6764.

Merrot P., Juillot F., Noël V., Lefebvre P., Brest J., Menguy N., Guigner J.-M., Blondeau M., Viollier E., Fernandez J.-M., Moreton B., Bargar J. R. and Morin G. (2019) Nickel and iron partitioning between clay minerals, Fe-oxides and Fe-sulfides in lagoon sediments from New Caledonia. *Science of The Total Environment* **689**, 1212–1227.

Michel F. M., Antao S. M., Chupas P. J., Lee P. L., Parise J. B. and Schoonen M. A. A. (2005) Short- to Medium-Range Atomic Order and Crystallite Size of the Initial FeS Precipitate from Pair Distribution Function Analysis. *Chem. Mater.* **17**, 6246–6255.

Morin G., Juillot F., Casiot C., Bruneel O., Personné J.-C., Elbaz-Poulichet F., Leblanc M., Ildefonse P. and Calas G. (2003) Bacterial Formation of Tooeleite and Mixed Arsenic(III) or

Arsenic(V)−Iron(III) Gels in the Carnoulès Acid Mine Drainage, France. A XANES, XRD, and SEM Study. *Environ. Sci. Technol.* **37**, 1705–1712.

Morin G., Noël V., Menguy N., Brest J., Baptiste B., Tharaud M., Ona-Nguema G., Ikogou M., Viollier E. and Juillot F. (2017) Nickel accelerates pyrite nucleation at ambient temperature. *Geochem. Persp. Let.*, 6–11.

Morse J. W., Millero F. J., Cornwell J. C. and Rickard D. (1987) The chemistry of the hydrogen sulfide and iron sulfide systems in natural waters. *Earth-Science Reviews* **24**, 1–42.

Morse J. W. and Arakaki T. (1993) Adsorption and coprecipitation of divalent metals with mackinawite (FeS). , 6.

Morse J. W. (1994) Interactions of trace metals with authigenic sulfide minerals: implications for their bioavailability. *Marine Chemistry* **46**, 1–6.

Morse J. W. and Luther G. W. (1999) Chemical influences on trace metal-sulfide interactions in anoxic sediments. *Geochimica et Cosmochimica Acta* **63**, 3373–3378.

Mukherjee I., Large R. R., Bull S., Gregory D. G., Stepanov A. S., Ávila J., Ireland T. R. and Corkrey R. (2019) Pyrite trace-element and sulfur isotope geochemistry of paleo-mesoproterozoic McArthur Basin: Proxy for oxidative weathering. *American Mineralogist* **104**, 1256–1272.

Mullet M., Boursiquot S., Abdelmoula M., Génin J.-M. and Ehrhardt J.-J. (2002) Surface chemistry and structural properties of mackinawite prepared by reaction of sulfide ions with metallic iron. *Geochimica et Cosmochimica Acta* **66**, 829–836.

Neretin L. N., Böttcher M. E., Jørgensen B. B., Volkov I. I., Lüschen H. and Hilgenfeldt K. (2004) Pyritization processes and greigite formation in the advancing sulfidization front in the upper Pleistocene sediments of the Black Sea 1 1Associate editor: D. Canfield. *Geochimica et Cosmochimica Acta* **68**, 2081–2093.

Niazi N. K. and Burton E. D. (2016) Arsenic sorption to nanoparticulate mackinawite (FeS): An examination of phosphate competition. *Environmental Pollution* **218**, 111–117.

Noël V. (2014) Speciation of iron and nickel in the mangrove sediments downstream lateritized ultramafic watershed (New Caledonia). Available at: https://tel.archives-ouvertes.fr/tel-01140282.

Noël V., Morin G., Juillot F., Marchand C., Brest J., Bargar J. R., Muñoz M., Marakovic G., Ardo S. and Brown G. E. (2015) Ni cycling in mangrove sediments from New Caledonia. *Geochimica et Cosmochimica Acta* **169**, 82–98.

Noel V., Kumar N., Boye K., Barragan L., Lezama-Pacheco J., Chu R. K., Tolic N., Brown G. and Bargar J. (2020) FeS Colloids – Formation and Mobilization Pathways in Natural Waters. *Environ. Sci.: Nano*, 10.1039.C9EN01427F.

Ohfuji H. and Rickard D. (2006) High resolution transmission electron microscopic study of synthetic nanocrystalline mackinawite. *Earth and Planetary Science Letters* **241**, 227–233.

Pédrot M., Dia A., Davranche M., Bouhnik-Le Coz M., Henin O. and Gruau G. (2008) Insights into colloid-mediated trace element release at the soil/water interface. *Journal of Colloid and Interface Science* **325**, 187–197.

Phan V. T. H., Bardelli F., Le Pape P., Couture R.-M., Fernandez-Martinez A., Tisserand D., Bernier-Latmani R. and Charlet L. (2019) Interplay of S and As in Mekong Delta sediments during redox oscillations. *Geoscience Frontiers* **10**, 1715–1729.

Picard A., Gartman A., Clarke D. R. and Girguis P. R. (2018) Sulfate-reducing bacteria influence the nucleation and growth of mackinawite and greigite. *Geochimica et Cosmochimica Acta* **220**, 367–384.

Planer-Friedrich B. (2020) Comment on “Thioarsenite Detection and Implications for Arsenic Transport in Groundwater.” *Environ. Sci. Technol.* **54**, 7730–7731.

Ravel B. and Newville M. (2005) ATHENA, ARTEMIS, HEPHAESTUS: data analysis for X-ray absorption spectroscopy using IFEFFIT. *J Synchrotron Rad* **12**, 537–541.

Rettig S. J. and Trotter J. (1987) Refinement of the structure of orthorhombic sulfur, α-S8. *Acta Cryst C* **43**, 2260–2262.

Rickard D. T. (1975) Kinetics and mechanism of pyrite formation at low temperatures. *American Journal of Science* **275**, 636–652.

Rickard D. (1997) Kinetics of pyrite formation by the H2S oxidation of iron (II) monosulfide in aqueous solutions between 25 and 125°C: The rate equation. *Geochimica et Cosmochimica Acta* **61**, 115–134.

Rickard D. and Morse J. W. (2005) Acid volatile sulfide (AVS). *Marine Chemistry* **97**, 141–197.

Rickard D. and Luther G. W. (2007) Chemistry of Iron Sulfides. *Chem. Rev.* **107**, 514–562.

Saunders J. A., Lee M.-K., Dhakal P., Ghandehari S. S., Wilson T., Billor M. Z. and Uddin A. (2018) Bioremediation of arsenic-contaminated groundwater by sequestration of arsenic in biogenic pyrite. *Applied Geochemistry* **96**, 233–243.

Savage K. S., Tingle T. N., O'Day P. A., Waychunas G. A. and Bird D. K. (2000) Arsenic speciation in pyrite and secondary weathering phases, Mother Lode Gold District, Tuolumne County, California. *Applied Geochemistry* **15**, 1219–1244.

Scholz F. and Neumann T. (2007) Trace element diagenesis in pyrite-rich sediments of the Achterwasser lagoon, SW Baltic Sea. *Marine Chemistry* **107**, 516–532.

Schoonen M. A. A. and Barnes H. L. (1988) An approximation of the second dissociation constant for H2S. *Geochimica et Cosmochimica Acta* **52**, 649–654.

Seder-Colomina M., Mangeret A., Stetten L., Merrot P., Diez O., Julien A., Barker E., Thouvenot A., Bargar J., Cazala C. and Morin G. (2018) Carbonate Facilitated Mobilization of Uranium from Lacustrine Sediments under Anoxic Conditions. *Environ. Sci. Technol.* **52**, 9615–9624.

Shannon R. D. (1976) Revised effective ionic radii and systematic studies of interatomic distances in halides and chalcogenides. *Acta Cryst A* **32**, 751–767.

Stetten L., Blanchart P., Mangeret A., Lefebvre P., Le Pape P., Brest J., Merrot P., Julien A., Proux O., Webb S. M., Bargar J. R., Cazala C. and Morin G. (2018) Redox Fluctuations and Organic Complexation Govern Uranium Redistribution from U(IV)-Phosphate Minerals in a Mining-Polluted Wetland Soil, Brittany, France. *Environ. Sci. Technol.* **52**, 13099–13109.

Swanner E. D., Webb S. M. and Kappler A. (2019) Fate of cobalt and nickel in mackinawite during diagenetic pyrite formation. *American Mineralogist* **104**, 917–928.

Teo B. K. (1986) Exafs: Basic Principles and Data Analysis. Available at: https://www.semanticscholar.org/paper/Exafs%3A-Basic-Principles-and-Data-Analysis-Teo/5698a4ba3944d6eaf75511547bc9b5dea1fdc18c [Accessed May 4, 2020].

Theberge S. M. and Luther III G. W. (1997) Determination of the Electrochemical Properties of a Soluble Aqueous FeS Species Present in Sulfidic Solutions. *Aquatic Geochemistry* **3**, 191–211.

Thomas H. V., Large R. R., Bull S. W., Maslennikov V., Berry R. F., Fraser R., Froud S. and Moye R. (2011) Pyrite and Pyrrhotite Textures and Composition in Sediments, Laminated Quartz Veins, and Reefs at Bendigo Gold Mine, Australia: Insights for Ore Genesis. *Economic Geology* **106**, 1–31.

Tribovillard N., Algeo T. J., Lyons T. and Riboulleau A. (2006) Trace metals as paleoredox and paleoproductivity proxies: An update. *Chemical Geology* **232**, 12–32.

Tribovillard N. (2020) Arsenic in marine sediments: how robust a redox proxy? *Palaeogeography, Palaeoclimatology, Palaeoecology*, 109745.

Vaughan D. J. and Ridout M. S. (1971) Mössbauer studies of some sulphide minerals. *Journal of Inorganic and Nuclear Chemistry* **33**, 741–746.

Watson J. H. P., Cressey B. A., Roberts A. P., Ellwood D. C., Charnock J. M. and Soper A. K. (2000) Structural and magnetic studies on heavy-metal-adsorbing iron sulphide nanoparticles produced by sulphate-reducing bacteria. *Journal of Magnetism and Magnetic Materials* **214**, 13–30.

Webb S. M. (2005) SIXpack: a graphical user interface for XAS analysis using IFEFFIT. *Phys. Scr.* **2005**, 1011.

Wei D. and Osseo-Asare K. (1997) Aqueous synthesis of finely divided pyrite particles. *Colloids and Surfaces A: Physicochemical and Engineering Aspects* **121**, 27–36.

Wilke M., Farges F., Petit P.-E., Brown G. E. and Martin F. (2001) Oxidation state and coordination of Fe in minerals: An Fe K-XANES spectroscopic study. *American Mineralogist* **86**, 714–730.

Wilkin R. T. and Barnes H. L. (1996) Pyrite formation by reactions of iron monosulfides with dissolved inorganic and organic sulfur species. *Geochimica et Cosmochimica Acta* **60**, 4167–4179.

Wilkin R. T. and Beak D. G. (2017) Uptake of nickel by synthetic mackinawite. *Chemical Geology* **462**, 15–29.

Wilkin R. T., Ford R. G., Costantino L. M., Ross R. R., Beak D. G. and Scheckel K. G. (2019) Thioarsenite Detection and Implications for Arsenic Transport in Groundwater. *Environ. Sci. Technol.* **53**, 11684–11693.

Wolthers M., Gaast S. J. V. der and Rickard D. (2003) The structure of disordered mackinawite. *American Mineralogist* **88**, 2007–2015.

Wolthers M., Charlet L., van Der Weijden C. H., van der Linde P. R. and Rickard D. (2005) Arsenic mobility in the ambient sulfidic environment: Sorption of arsenic(V) and arsenic(III) onto disordered mackinawite. *Geochimica et Cosmochimica Acta* **69**, 3483–3492.

Wolthers M., Butler I. B. and Rickard D. (2007) Influence of arsenic on iron sulfide transformations. *Chemical Geology* **236**, 217–227.

Zhang J., Kim H. and Townsend T. (2014) Methodology for assessing thioarsenic formation potential in sulfidic landfill environments. *Chemosphere* **107**, 311–318.

Zhang J., Ren D., Zheng C., Zeng R., Chou C.-L. and Liu J. (2002) Trace element abundances in major minerals of Late Permian coals from southwestern Guizhou province, China. *International Journal of Coal Geology* **53**, 55–64.

Appendix

****

Influence of trace level As or Ni on pyrite formation kinetics at low temperature

Baya C.[1], Le Pape P.[1]*, Baptiste B.[1], Brest J.[1], Landrot G.[2], Elkaïm E.[2], Noël V.[3], Blanchard M.[4], Ona-Nguema G.[1], Juillot F.[1,5], Morin G.[1]

6. Institut de Minéralogie, de Physique des Matériaux et de Cosmochimie (IMPMC), UMR 7590 CNRS-Sorbonne Université-IRD-MNHN, case 115, 4 place Jussieu, 75252 Paris Cedex 5, France.
7. Synchrotron SOLEIL, F-91192 Gif Sur Yvette, France
8. Stanford Synchrotron Radiation Lightsource, SLAC National Accelerator Laboratory, 2575 Sand Hill Road, MS 69, Menlo Park, CA 94025, USA
9. Géosciences Environnement Toulouse (GET), Université de Toulouse, CNRS, IRD, UPS, CNES, 14, Avenue Edouard Belin, 31400 Toulouse, France.
10. Institut de Recherche pour le Développement (IRD), UMR 206/UMR 7590 IMPMC, 98848 Nouméa, New Caledonia

January, 10th 2020,
Revised version submitted to
Geochimica et Cosmochimica Acta

***Corresponding author**: pierre.le_pape@upmc.fr

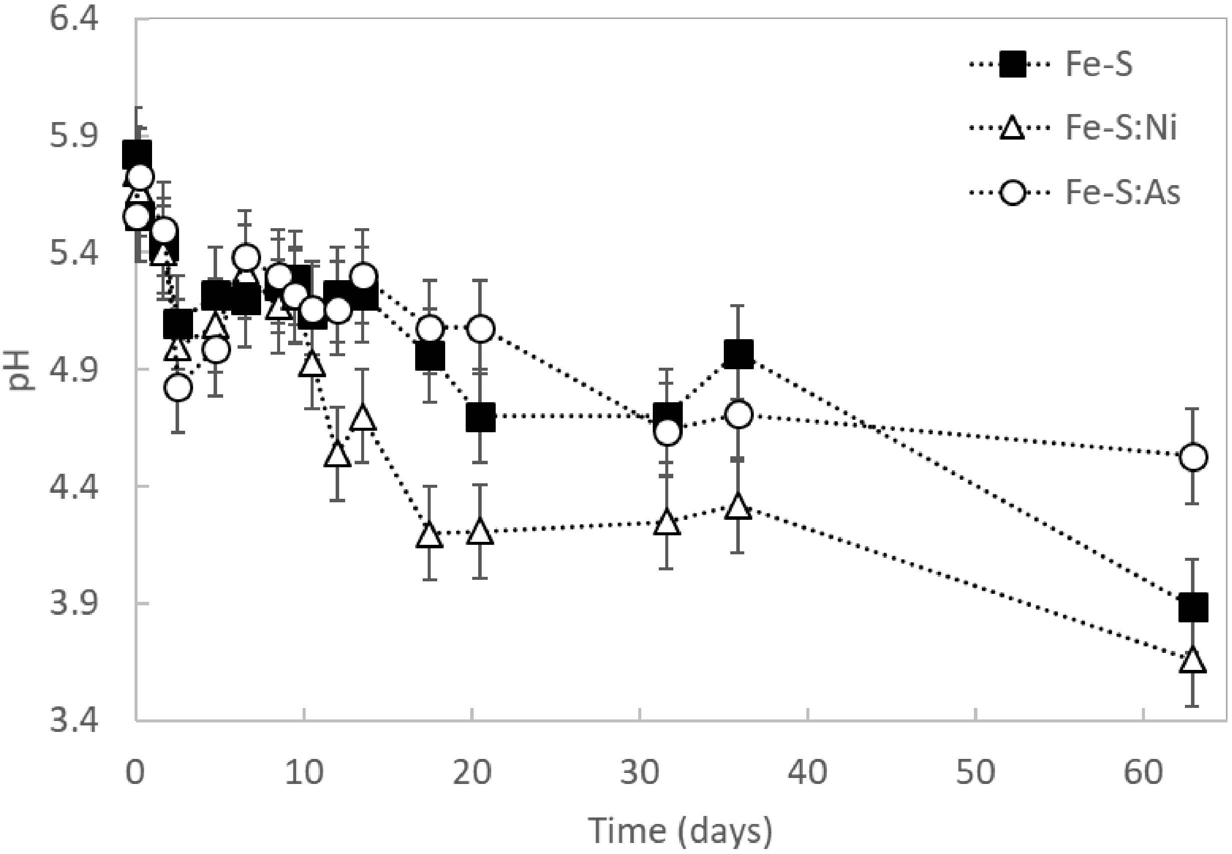

Figure SI-1. Evolution of the pH in each experiment over time. Each data point corresponds to an independent pH measurement performed in the glove box. The pH of the Fe-S solution is represented by black squares, of the Fe-S:Ni solution by white triangles and of the Fe-S:As solution by white circles. The points are linked by dotted lines to help the reader's comprehension. The values are reported in Table SI-1. Uncertainties are carefully estimated to be 0.2 pH units for each measurement at maximum.

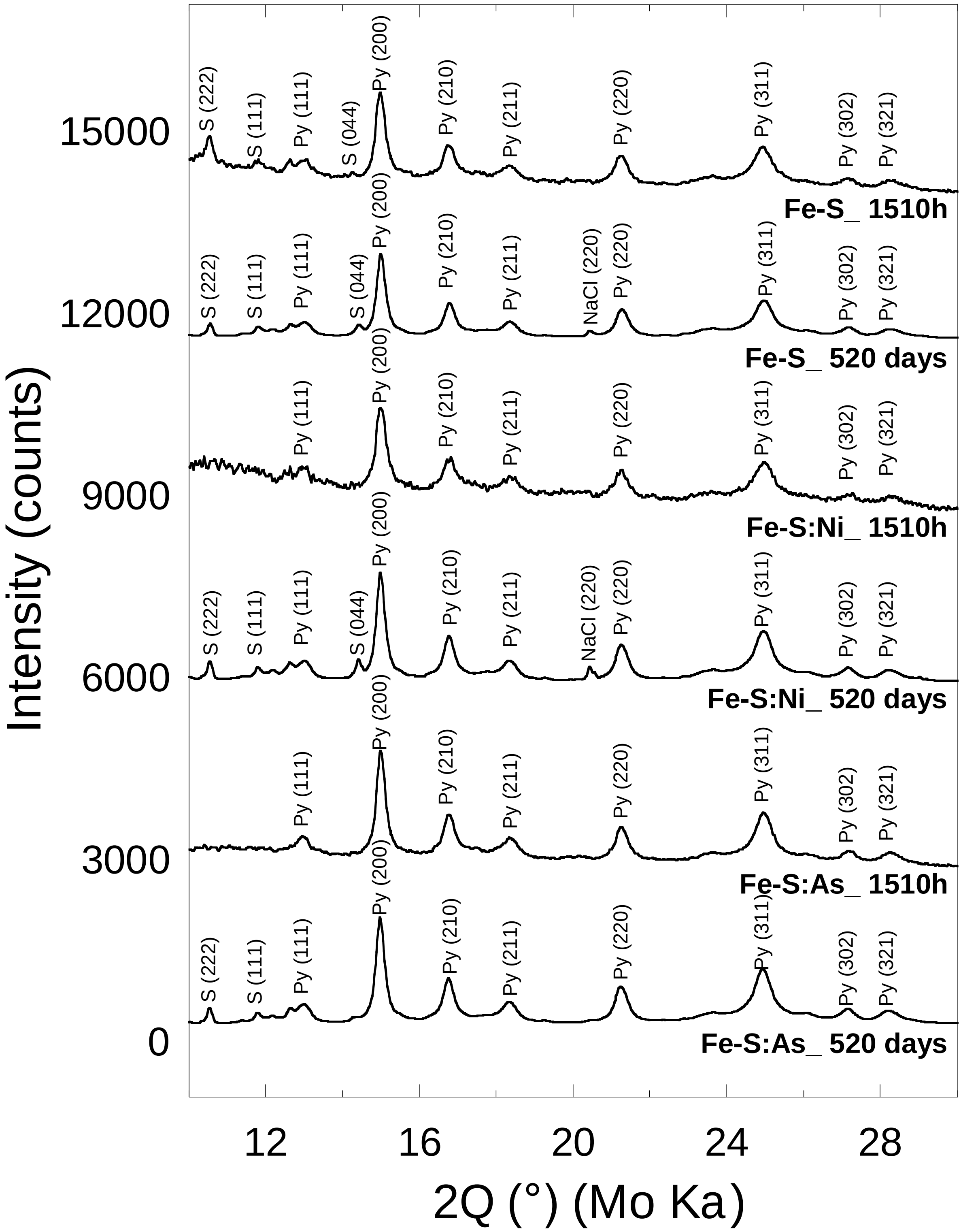

Figure SI-2. XRD powder patterns of the solids collected at 1510 hours and at the end of the pyrite synthesis (520 days) in the absence or presence of aqueous Ni or As, with a Ni:Fe or As:Fe ratio of 0.001 mol:mol in the starting solution. S: α-sulfur; Py: pyrite. Note the similar line-width for pyrite at 1510h and 520 days, indicating that aging did not significantly affected the crystallites size.

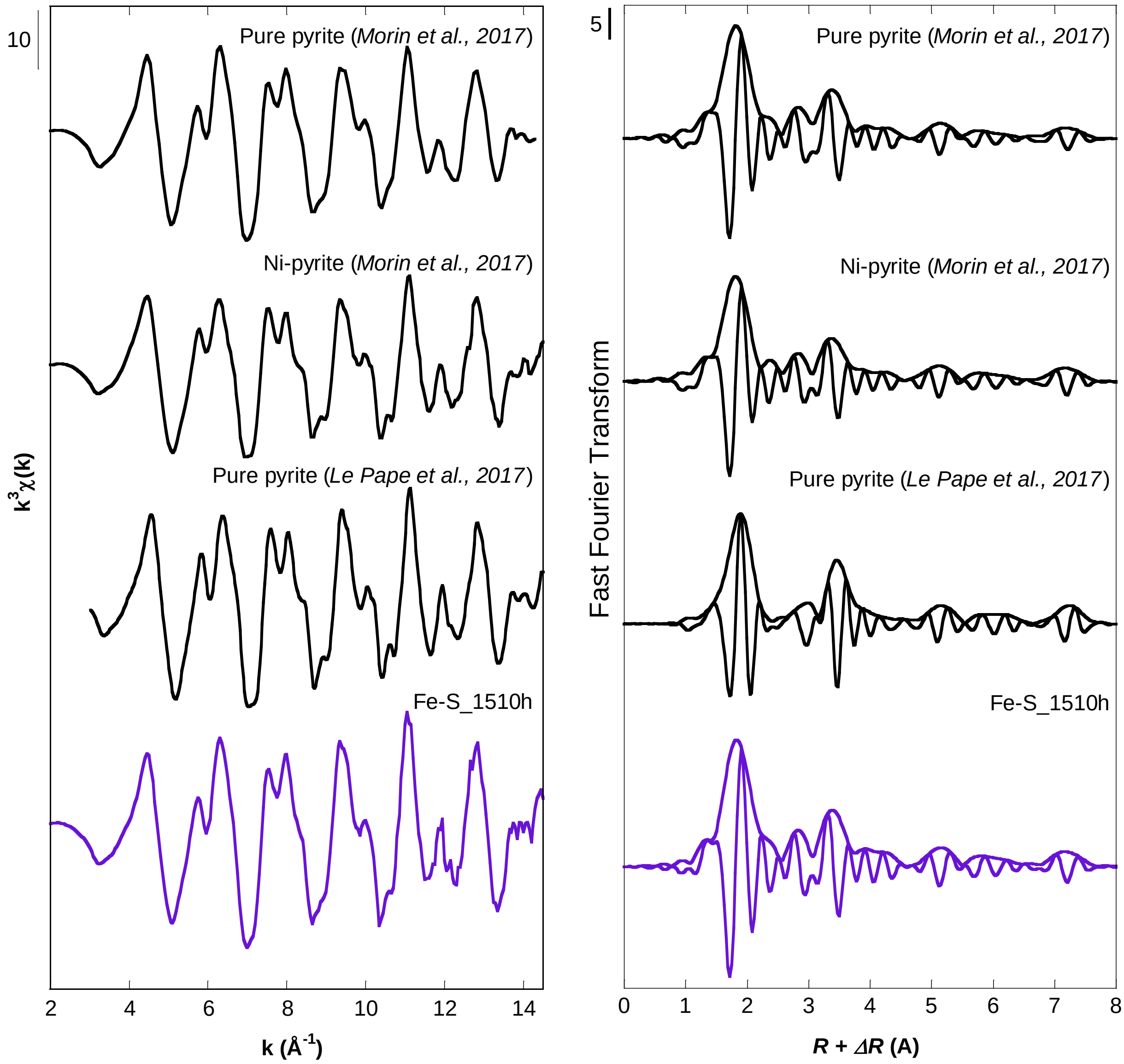

Figure SI-3. Fe *K*-edge EXAFS spectra of pyrite samples taken from the literature (Morin et al., 2017; Le Pape et al., 2017) with that of our Fe-S_1510h sample, confirming that this sample of the Fe:S control synthesis corresponds to pyrite.

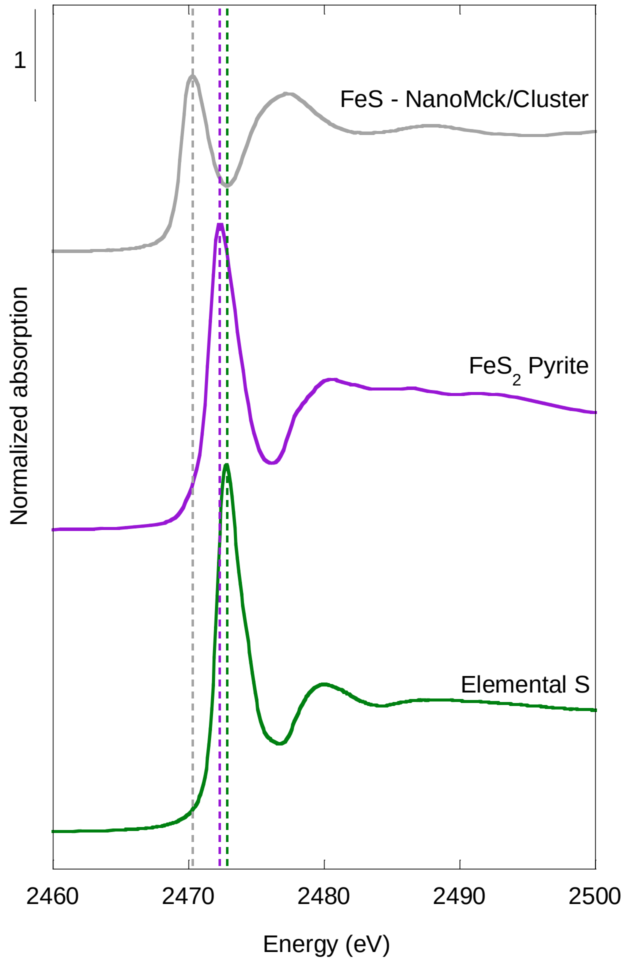

Figure SI-4. S *K*-edge XANES spectra of the model compounds used to fit our experimental data (Figure 3). FeS – NanoMck/Cluster (in grey) corresponds to a sample fully described in Ikogou et al. (2017). FeS_2 Pyrite (in purple) and elemental S (S(0)) (in green) were measured at the 4-3 beamline at SSRL (CA, USA).

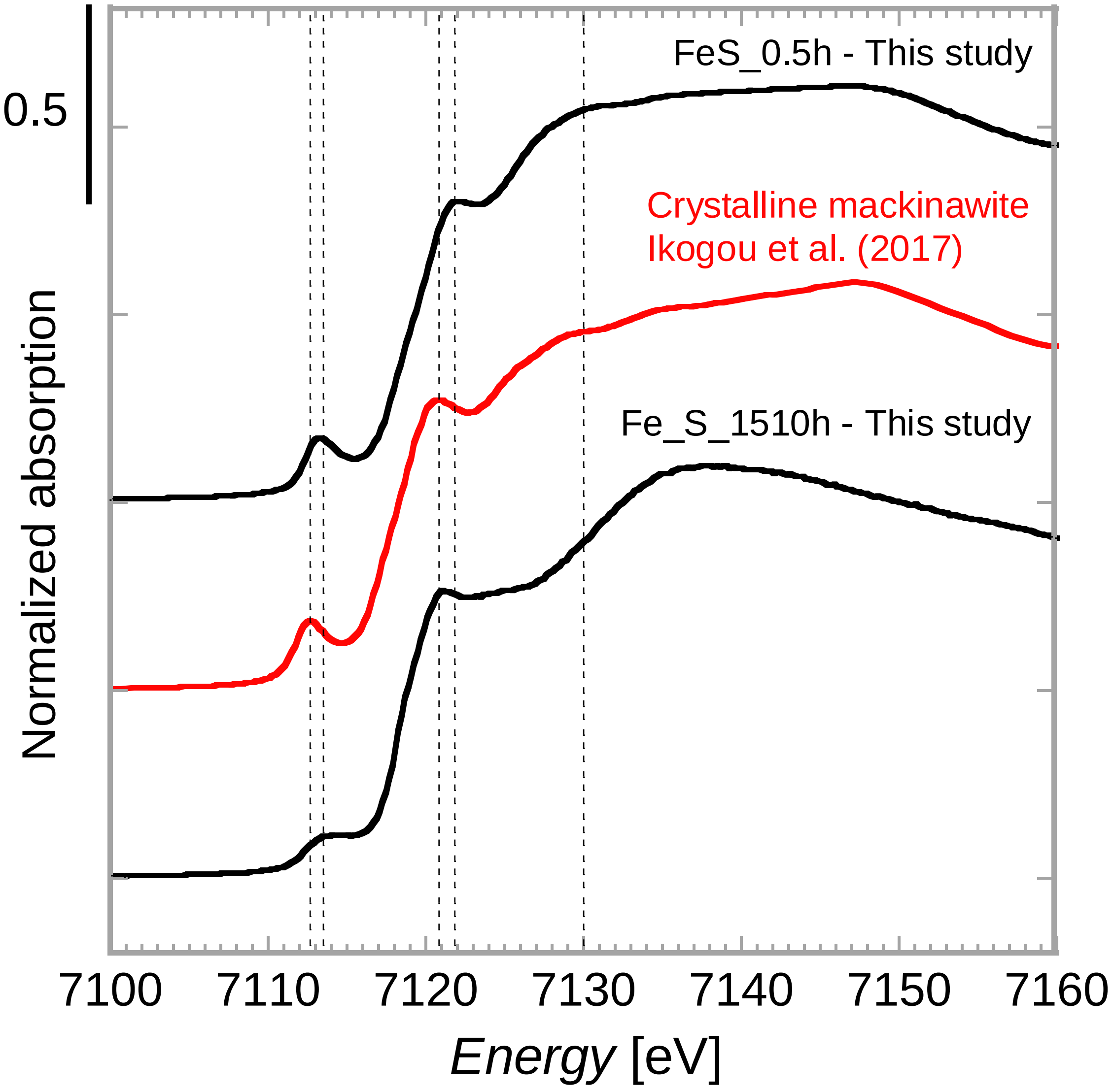

Figure SI-5. Comparison of the Fe *K*-edge XANES spectra of Fe-S_0.5h (corresponding to FeS precursors, in black on the top), Fe-S_1510h (pyrite, in black on the bottom) and crystalline mackinawite (in red, “FeS + Ni – 3.5months“ sample in the study by Ikogou et al. (2017)).

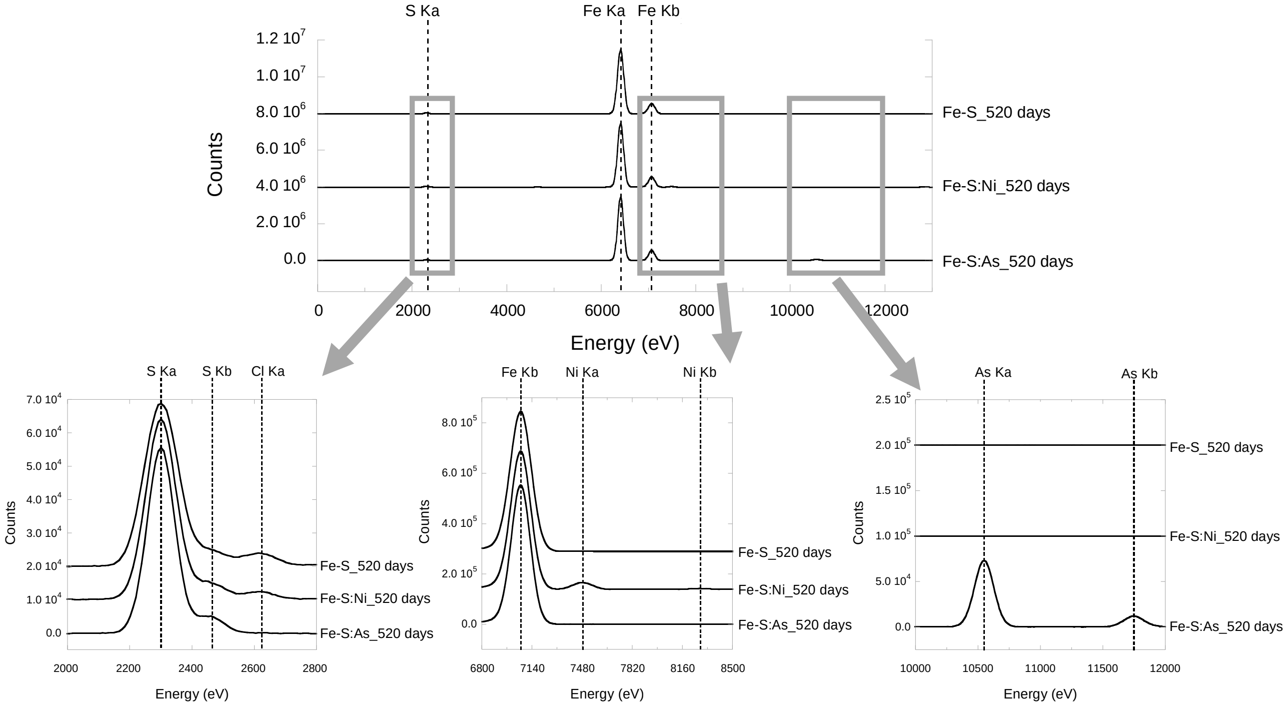

Figure SI-6. X-Ray Fluorescence (XRF) spectra from the final samples from each synthesis over the 0–13000 eV energy range. Below, zoomed-in sections of these XRF spectra show the signals around the S Kα, Ni Kα and As Kα emission lines (from left to right). These analyses were performed to estimate the Fe, S, Ni and As contents of the final samples. In the Ni-doped sample (Fe-S:Ni_520 days) and As-doped sample (Fe-S:As_520 days), an increase of the corresponding element's characteristic peaks is detectable. Data were collected at ambient temperature in air with a Si-drift KETEK™ detector using a Mo rotating anode source ($\lambda_{K\alpha1}$=0.709319 Å, $\lambda_{K\alpha2}$=0.713609 Å) equipped with Varimax focusing optics. The beam size was set to 100 µm on pure 3mm-diameter pellets and the acquisition lasted 1 hour per sample.

Time (days)	**Fe-S**	**Fe-S:Ni**	**Fe-S:As**
0	5.8	5.7	5.6
0.02	5.6	5.7	5.7
1.6	5.4	5.4	5.5
2.5	5.1	5	4.8
4.75	5.2	5.1	5
6.5	5.2	5.3	5.4
8.5	5.3	5.2	5.3
9.5	5.3	5.2	5.2
10.5	5.1	4.9	5.2
12	5.2	4.5	5.2
13.5	5.2	4.7	5.3
17.5	5	4.2	5.1
20.5	4.7	4.2	5.1
31.5	4.7	4.2	4.6
36	5	4.3	4.7
63	3.9	3.7	4.5

Table SI-1. pH values in each synthesis over time. Uncertainties are estimated to be 0.2 pH units of the measurement at maximum.

	Sample	**dFeS**	**NFeS**	**dFeFe**	**NFeFe**	χ^2_R
	Fe-S_0h	2.250(1)	2.8(1)	2.680(1)	1.68(2)	25.88
	Fe-S_0.5h	2.251(1)	2.98(5)	2.675(2)	1.74(4)	13.83
	Fe-S_40h	2.248(1)	3.01(3)	2.671(1)	1.74(2)	21.71
	Fe-S_60h	2.250(1)	3.17(2)	2.673(1)	1.9(2)	18.23
	Fe-S_156h	2.246(1)	2.91(3)	2.673(1)	1.81(3)	20.5
	Fe-S_252h	2.244(1)	2.97(4)	2.671(1)	1.88(4)	95.7
	Fe-S_288h	2.246(1)	3.32(3)	2.664(1)	1.82(3)	20.3
n = 7	**Fe-S average**	**2.248(1)**	**3.02(3)**	**2.672(1)**	**1.80(3)**	
	Fe-S standard deviation	**0.003(0)**	**0.17(1)**	**0.005(0)**	**0.080(9)**	
	Fe-S:Ni_0h	2.25(1)	3.01(5)	2.67(1)	1.61(5)	18.7
	Fe-S:Ni_40h	2.251(1)	2.99(2)	2.672(1)	1.71(2)	17.48
	Fe-S:Ni_60h	2.251(1)	3.14(5)	2.668(1)	1.85(5)	23.33
n = 3	**Fe-S:Ni average**	**2.251(1)**	**3.05(4)**	**2.670(1)**	**1.72(4)**	
	Fe-S:Ni standard deviation	**0.000(1)**	**0.08(2)**	**0.002(1)**	**0.12(2)**	
	Fe-S:As_0h	2.253(1)	2.86(3)	2.677(1)	1.70(3)	10.9
	Fe-S:As_40h	2.248(1)	2.97(2)	2.670(1)	1.60(2)	15.1
	Fe-S:As_60h	2.247(2)	2.87(6)	2.674(2)	1.60(5)	38.9
	Fe-S:As_252h	2.247(1)	2.98(5)	2.674(1)	1.75(4)	55.01
	Fe-S:As_288h	2.249(1)	3.04(3)	2.667(1)	1.80(2)	19.53
	Fe-S:As_324h	2.248(1)	3.04(4)	2.666(1)	1.77(4)	18.6
	Fe-S:As_492h	2.252(1)	2.83(4)	2.672(1)	1.73(3)	55.31
n = 7	**Fe-S:As average**	**2.249(1)**	**2.94(4)**	**2.671(1)**	**1.71(3)**	
	Fe-S:As standard deviation	**0.002(0)**	**0.09(3)**	**0.004(0)**	**0.08(1)**	

		Average on all samples	**Standard deviation on all samples**
n=17	**dFeS**	2.248	0.002
	NFeS	2.9	0.1
	dFeFe	2.671	0.004
	NFeFe	1.74	0.09

Table SI-2. Results of the shell-by-shell fitting procedures performed on the Fe *K*-edge data for the two first shells of atom (Fe-S and Fe-Fe), and for all the samples prior to pyrite formation (see Figure 1 main text). d stands for the interatomic distance between the absorbing atom and the neighbouring shell, N is the number of atomic neighbours in the shell, n is the number of samples used to average the interatomic distances and number of atomic neighbours. The goodness of fit was estimated by a reduced chi-square indicator χ^2_R. For this particular analysis, the Debye-Waller factors were fixed on the basis of the best fit obtained on sample Fe-S_0.5h (DWFeS=0.064 and DWFeFe=0.067).